ISSN 1063-780X, Plasma Physics Reports, 2024, Vol. 50, No. 4, pp. 470–492. © Pleiades Publishing, Ltd., 2024.

TOKAMAKS

The Concept of the MSE Diagnostic at the TRT Tokamak Facility

I. A. Zemtsov[a,b,*] (ORCID: 0000-0002-7056-0105), V. S. Neverov[a] (ORCID: 0000-0001-9519-9750), A. R. Nemets[a] (ORCID: 0000-0002-3163-7288), V. A. Krupin[a], A. A. Pshenov[c] (ORCID: 0000-000-8527-5940), V. I. Davydenko[d], and N. V. Stupishin[d]

[a] *National Research Center Kurchatov Institute, Moscow, 123098 Russia*
[b] *Bauman Moscow State Technical University, Moscow, 105005 Russia*
[c] *ITER Organization, Route de Vinon-sur-Verdon, St. Paul Lez Durance Cedex, France*
[d] *Budker Institute of Nuclear Physics, Siberian Branch, Russian Academy of Sciences, Novosibirsk, 630090 Russia*
**e-mail: zemtsov_ia@nrcki.ru*

Received December 6, 2023; revised January 10, 2024; accepted January 20, 2024

Abstract—The possibility of carrying out measurements of plasma parameters in a tokamak with reactor technologies (TRT) by means of the technique based on the Stark effect by resolving the spectrum of the split lines of Balmer series emitted by fast hydrogen atoms injected into plasma is analyzed. The code containing the models of emission applicable for the high-temperature tokamak plasma, along with the library of functions for the ray-tracing simulation of geometric optics, was used. Simulation of spectra of active neutral beam emission and plasma emission, both as a result of charge exchange on beam atoms and passive one, taking into account reflections from the plasma facing vessel elements, allowed determining parameters of the diagnostic injector and relative position of the light-collection systems and heating injectors for which the useful and background spectra could be separated. The signal gathered by the detector is simulated. The shape of the visual angle along the line of sight, optical properties of the lens materials, the instrumental function of the spectral device, the sensor characteristics, and statistical noise of the signal are taken into consideration. Based on the obtained results, a preliminary concept of the motional Stark effect (MSE) diagnostic for the tokamak with reactor technologies is proposed.

Keywords: thermonuclear fusion, tokamak, TRT, plasma diagnostics, MSE diagnostics, spectroscopy

DOI: 10.1134/S1063780X24600130

1. INTRODUCTION

The project of the tokamak with reactor technologies (TRT) represents the next step in development of the program aimed at realization of controlled fusion. The TRT is a large-scale facility for magnetic confinement of high-temperature plasma. It exceeds the international experimental facility (ITER) that is currently at the final stage of its construction with respect to certain parameters. The TRT mission consists in development and integration of the key thermonuclear technologies, development and investigation of long ($\geq$100 s) quasi-stationary discharges in the tokamak plasma with temperature and density close to those required for the fusion reactor, along with obtaining and studying the thermonuclear plasma in which heating by alpha-particles is dominant in the near-axial region of the plasma column in the deuterium–tritium experiments [1].

To achieve these goals, the tokamak has to be equipped with an advanced diagnostic complex that would allow conducting measurements of the required plasma parameters. Measurements of profiles of the plasma current density $j(\rho)$ and the safety factor $q(\rho)$ that determine stability of the plasma column, along with the heat and particle transfer in plasma, are critically important for realization of the TRT goals. Knowing these parameters at the initial stages of system operation is needed for development of the discharge scenarios and selection of parameters of the plasma-control systems. At later stages, such a knowledge will be required for understanding the processes that have to be controlled in order to obtain tokamak discharges with long energy-confinement times τ_E and high values of parameter β_N that is defined as the ratio of the gas-dynamic pressure to the magnetic one.

The sought-for quantities listed above can be determined from measurements of the pitch angle of magnetic field $\gamma_{\text{pitch}} = \tan^{-1}(B_\theta/B_\varphi)$. The common method of determining this parameter consists in analysis of the direction of polarization of the Balmer series line emitted by fast atoms propagating through a magnetic field. This technique is referred to as the Motional Stark Effect (MSE) diagnostic, since substantial splitting of components of this line that allows conducting the necessary measurements occurs due to the motional Stark effect [2–6].

This work aims at development of the concept of the MSE diagnostic for the TRT based on the MSE-LS spectroscopic technique described in the next section. Special attention is paid to simulation of the signals that will be detected by the MSE-diagnostic instruments, which is necessary for determining the observation geometry and parameters of the measuring equipment in the first place. The synthesized signals can also be used for solving the inverse problem in order to determine the location from which the signal has to be collected, the operating range of the diagnostic, and its uncertainty.

In the simplest case, the inverse problem of reconstruction of the local value of B_θ/B_φ from the MSE spectrum reduces to fitting the experimental spectrum by a set of Gaussian functions. Each of them describes its own component of the split spectrum. In the process, the widths of the components are also fitted independently, since the further away the component from the line center, the larger its broadening. The line-of-sight geometry and the geometry of the diagnostic beam are assumed to be known. The magnitude of the Stark splitting of the line depends on projection of the vector of magnetic induction on the direction perpendicular to the vector of atomic velocity (see Eq. (2) below), while the ratio of the spectral components polarized along the Lorentz electric field $\mathbf{E_L}$ to spectral components polarized perpendicular to $\mathbf{E_L}$ depends on the angle between vector $\mathbf{E_L}$ and the direction of observation (see Eq. (9) below). Hence, by fitting the positions and the relative intensities of the spectral components, the local value of B_θ/B_φ can be reconstructed. The mathematical formulation and solution of the inverse problem within the framework of the synthetic diagnostic for estimating the accuracy of the measured quantity γ_{pitch} will be the subject of a separate publication.

2. PHYSICAL FOUNDATIONS OF THE MSE DIAGNOSTIC

The effect observed when a Lorentz electric field appearing in the frame of reference associated with an atom is acting upon an atom moving in a magnetic field is referred to as the motional Stark effect. The vector of this field is given by

$$\mathbf{E_L} = \mathbf{v} \times \mathbf{B}, \tag{1}$$

where $\mathbf{v}$ is the vector of atom's velocity, and $\mathbf{B}$ is the vector of magnetic induction. The details regarding the Stark effect can be found in, e.g., [7], while the physical foundations of the MSE diagnostic are described in [2–6]. We provide a brief description of both below.

The effect consists in partial lifting of degeneracy of the excited atomic states and splitting of its electron terms. As a result, the lines in the optical spectra of an atom (ion) emission split into components exhibiting different polarization. The components polarized parallel to vector $\mathbf{E_L}$ are denoted as the π-components, while those polarized perpendicular to vector $\mathbf{E_L}$ are denoted as the σ-components. The magnitude of splitting for the hydrogen-like atoms is proportional to the magnitude of the electric field. In the case of transitions associated with the Balmer series in a hydrogen atom (H_α) with $n = 3 \to 2$, the level with the principal quantum number $n = 3$ splits into 5 energy levels, while the level with $n = 2$ splits into 3 energy levels. Taking selection rules into account, there appear a total of 15 main transitions (see, e.g., expressions (2.12)–(2.14) in [2]), but only 9 of them can be resolved when obtaining the spectra. The relative intensities of the other Stark lines are so low (0.02–0.3% of the integral line intensity) that their contribution can be neglected. The diagram of the split spectrum calculated for the H_α line of the hydrogen atom is presented in Fig. 1.

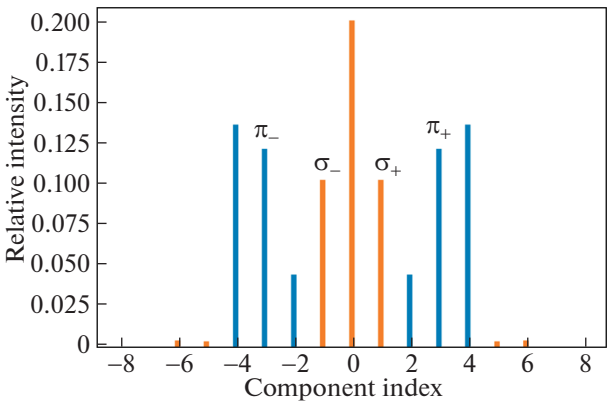

Fig. 1. Component composition of the MSE spectrum of a hydrogen atoms at electron density of 10^{19} m^{-3} and beam energy of 100 keV.

Application of the Stark effect in the experiments carried out on tokamaks is usually based on injection of a beam of fast atoms formed by the heating and/or diagnostic injectors. The spectrum of the induced emission of atoms of hydrogen (deuterium) is measured and analyzed. The magnitude of the Stark line splitting $\Delta\lambda_{\text{Stark}}$ can be expressed as a function of projection of the magnetic field on the direction perpendicular to the vector of atom's velocity $B_\perp$ (see expression (2.14) in [4]):

$$\Delta\lambda_{\text{Stark}} \approx \frac{3ea_0}{2hc}\lambda_0^2 v B_\perp, \tag{2}$$

where a_0 is the Bohr radius, e is the electron charge, h is the Planck constant, c is the speed of light, v is the atom's velocity, and λ_0 is the wavelength associated with the line of hydrogen (deuterium) in the absence of splitting.

When the beam direction and the geometry chosen for its observation are known, measurement of the spectral characteristics of the H_α line of the diagnostic (or heating) beam with an adequate spectral resolution allows determining the local magnitude of γ_{pitch}.

The following variants of the MSE diagnostic are currently used in the experiments carried out on tokamaks: polarimetric (the Line-Polarization, or MSE-LP) and spectroscopic (the Line-Shift, or MSE-LS). The former are based on the measurement of the direction of the polarization vector of light directly by means of the modulating polarizers. The latter ones gather information on the direction of the polarization vector from the measurements of the magnitude of spectral splitting and the relation between intensities of the π- и σ-components of the Stark spectrum. The Imaging MSE method represents a relatively new type of the MSE measurements. It is based on analysis of the two-dimensional interferograms of the polarized plasma emission.

Each of the named methods has its advantages and limitations. For example, the MSE-LP systems are fast and allow carrying out measurements in real time. Therefore, they can be used in the feedback loops for controlling the plasma discharge. However, such systems are based on using the ultra-narrow bandpass filters with transmission bandwidth of about 1 Å. In addition, the polarimeters used in such systems are sensitive to the neutron fluxes. The detection systems based on the MSE-LS method are more stable with respect to the action of plasma since the influence of perturbations of the vector of polarization of the radiation by the optical elements of the system, along with the Faraday effect, are eliminated. At the same time, such systems are subjected to the considerable reduction in light transmission due to contamination and degradation of the optical elements of the light collection and transmission systems caused by the gamma radiation and neutron fluxes. The Imaging MSE technique favorably stands out due to the possibility of carrying out two-dimensional spatial measurements of the angular distribution of polarization of emission and the fact that there is no need for separation of the components of the Stark spectrum. In addition, the signal-to-noise ratio obtained using this technique is higher. The drawbacks of the Imaging MSE method consist in complexity of its technical implementation and extremely high cost of its components [5, 6].

Based on the expected neutron fluxes, it is anticipated that carrying out measurement by means of the MSE-LP method at later stages of the TRT tokamak operation will be very difficult. A very high accuracy of the measurements conducted by means of the MSE-LS method can be expected since the design value of magnitude of the magnetic induction at the axis of the plasma column will induce large splitting of the active MSE spectrum. It should be noted that the neutron flux will be absent at the initial stages of system operation, which will allow carrying out measurements using the MSE-LP technique by mounting a photoelastic modulator (PEM) in one of the diagnostic ports close to plasma. Simultaneous use of two techniques will allow performing sufficiently accurate and detailed calibration of the results of operation of the MSE-LS diagnostic using more reliable measurements carried out by means of the PEM.

The MSE-LS diagnostic includes several main elements listed below.

(1) A diagnostic injector of the hydrogen atoms (DNB) that serves for injection of a beam of fast hydrogen atoms into plasma. Analysis of the emission spectrum of these atoms induced in plasma allows determining γ_{pitch}. The intensity of the active emission that will be driven in the plasma volume will be determined by injector parameters.

(2) The light collection system. Its characteristics determine the amount of light that will be transmitted by the fiber-optic collectors from plasma to the spectral device and the region of observation.

(3) The spectral device and detector. These devices are planned to be installed in a separate remote room and are used for selection of the spectral range of interest and its detection. Parameters of these devices determine the spectral resolution of the obtained spectrum and the uncertainty of the measured parameters.

In the present work, we present calculated parameters of all three parts of the MSE diagnostic.

3. SIMULATION OF THE MSE SPECTRUM

We used a set of tools for simulation of plasma parameters and processes occurring in it. The main instrument for performing calculations was a combination of the Cherab [8] and Raysect [9] codes. The obtained results were processed in the Python environment.

3.1. Mathematical Model Used in the Calculations

The models from the Cherab code used in the present work are described below. All of them, except for the model of the bremsstrahlung, were improved for this work.

3.1.1. The model of the neutral beam. We used the model of a monoenergetic Gaussian beam (i.e., the beam in which the density in the direction perpendicular to the injection axis is described by the Gaussian function) with attenuation along the beam-propaga-

tion direction. The density of atoms in the beam in the coordinate system of the beam had the following form:

$$n_H^{(\mathrm{Beam})} = \frac{R_H}{2\pi v_0 \sigma_x(z)\sigma_y(z)} \times \exp\left(-\frac{1}{2}\left(\left(\frac{x}{\sigma_x(z)}\right)^2 + \left(\frac{y}{\sigma_y(z)}\right)^2\right)\right) \times \exp\left(-\int_0^z \frac{S^{(\mathrm{CR})}(z')}{v_0} dz'\right), \quad (3)$$

$$\sigma_x(z) = \sqrt{\sigma^2 + (z - z_f)^2 \tan^2(\alpha_x)}, \quad \sigma_y(z) = \sqrt{\sigma^2 + (z - z_f)^2 \tan^2(\alpha_y)}, \quad (4)$$

$$S^{(\mathrm{CR})}(z) = \sum_{i=1}^{m} Z_i n_i(z) S_i^{(\mathrm{CR})}\left(\epsilon_{\mathrm{int}}(z), n_{e,i}^{(\mathrm{eq})}(z), T_i(z)\right), \quad (5)$$

$$n_{e,i}^{(\mathrm{eq})}(z) = \frac{1}{Z_i}\sum_{j=1}^{m} Z_j^2 n_j(z), \quad (6)$$

where the z axis was set along the beam-propagation direction, R_H is the number of neutral atoms injected per unit time, v_0 is the magnitude of the vector of velocity of the beam atoms, z_f is the distance to the beam focus, σ is the standard deviation of the beam in focus, α_x and α_y are the beam divergence angles, m is the number of types of plasma ions, Z_i is the charge of the ith type of plasma ions, n_i is the density of ions of the ith type, $S_i^{(\mathrm{CR})}$ is the beam attenuation coefficient due to radiative-collisional interaction with the ith type of plasma ions and corresponding fraction of electrons (the processes of excitation and subsequent ionization of the beam atoms due to collisions with ions and electrons but not the charge-exchange processes were taken into consideration), ϵ_{int} is the kinetic energy of the beam atoms in the frame of reference where ions of the ith type are at rest, and T_i is the temperature of ions of the ith type. Coefficients $S_i^{(\mathrm{CR})}$ are calculated using the codes of the Atomic Data and Analysis Structure (ADAS) software package [10] and are available in the OpenADAS database.

The (non-normalized) direction of velocity of the beam neutral atoms in the coordinate system of the beam at $z > z_f$ is given by

$$e_x = x\frac{(z - z_f)^2 \tan^2(\alpha_x)}{\sigma^2 + (z - z_f)^2 \tan^2(\alpha_x)}, \quad e_y = y\frac{(z - z_f)^2 \tan^2(\alpha_y)}{\sigma^2 + (z - z_f)^2 \tan^2(\alpha_y)}, \quad e_z = z - z_f. \quad (7)$$

Components e_x, e_y, and e_z change sign at $z < z_f$.

The beam energy, power, standard deviation of the beam in focus, and divergences (α_x and α_y) at the origin of the coordinate system, along with the position of focus and the type of gas in the beam, represent the boundary conditions for beam description in the discussed model.

3.1.2. The model of the MSE spectral intensity. Emissivity at a point, or angular power density of radiation, of the H_α line caused by impact excitation of beam atoms by electrons and ions was calculated in the coordinate system of plasma using the following expression:

$$\varepsilon_{32}^{(\mathrm{Beam})} = \frac{1}{4\pi} n_H^{(\mathrm{Beam})} \sum_{i=1}^{m} Z_i n_i q_{32}^{(\mathrm{Beam})}\left(\epsilon_{\mathrm{int}}, n_{e,i}^{(\mathrm{eq})}, T_i\right), \quad (8)$$

where $q_{32}^{(\mathrm{Beam})}$ is the coefficient of photon emission of the H_α line due to interaction of beam atoms with the plasma ions of the ith type and the corresponding fraction of electrons the value of which was adapted from the ADAS database.

The spectral distribution of intensity at a point was calculated in the following way:

$$f_{32}(\lambda) = \left(\sin^2(\theta) I_\sigma^{(\mathrm{T})} + \cos^2(\theta)\right) \times \sum_{i=-1}^{1} I_\sigma^{(i)} f_{\mathrm{G}}(\lambda_i, \sigma_{\mathrm{G}}) + \sin^2(\theta) I_\pi^{(\mathrm{T})} \times \sum_{i=-4\ldots-2,2\ldots4} I_\pi^{(i)} f_{\mathrm{G}}(\lambda_i, \sigma_{\mathrm{G}}), \quad (9)$$

$$I_\sigma^{(\mathrm{T})} + I_\pi^{(\mathrm{T})} = 1, \quad \sum_{i=-1}^{1} I_\sigma^{(i)} = 1, \quad \sum_{i=-4\ldots-2,2\ldots4} I_\pi^{(i)} = 1, \quad (10)$$

$$\lambda_i = \frac{hc}{\epsilon_{\mathrm{ph}} + i\Delta\epsilon_{\mathrm{Stark}}}, \quad \epsilon_{\mathrm{ph}} = \frac{hc}{\lambda_{32}(1 + \mathbf{vl}/c)}, \quad (11)$$

$$\Delta\epsilon_{\mathrm{Stark}} = \frac{3\varepsilon_0 h^2}{4\pi m_e e^2} E, \quad \mathbf{E} = \mathbf{v} \times \mathbf{B}, \quad (12)$$

where θ is the angle between vector $\mathbf{E}$ of the electric field and the direction of observation; $I_\sigma^{(\mathrm{T})}$ and $I_\pi^{(\mathrm{T})}$ are the fractions of the sum of all σ- and π-polarized components in the total spectrum upon observation perpendicular to the direction of **E,** respectively; $I_\sigma^{(i)}$ and $I_\pi^{(i)}$ are the fractions of individual σ- and π-polarized components in $I_\sigma^{(\mathrm{T})}$ and $I_\pi^{(\mathrm{T})}$, respectively; f_{G} is the Gaussian distribution with respect to the wavelength of radiation with a center at λ_i and standard deviation of σ_{G}; $\Delta\epsilon_{\mathrm{Stark}}$ is the magnitude of the Stark splitting; $\mathbf{v}$ is the velocity of the beam atoms; $\mathbf{B}$ is the magnetic field; $\mathbf{l}$ is the direction of observation; λ_{32} is the wave-

length of the D_α line in the absence of magnetic field. Quantities, $I_\pi^{(T)}$, $I_\sigma^{(T)}$, $I_\sigma^{(i)}$, and $I_\pi^{(i)}$ are functions of the beam energy and electron density; their values were adapted from [11, 12].

Product **vl** determines the Doppler shift of the MSE spectrum relative to λ_{32} and, as a result, relative to the passive D_α line and the spectrum of radiation emitted by beam neutrals in charge-exchange reactions with plasma ions (the charge-exchange spectrum). The natural broadening of the spectrum is determined by the standard deviation of the beam and its divergence, along with variation of **B** along the line of sight. The latter causes stronger broadening of the components with larger index *i*. Contribution of the radial electric field the presence of which can have a negative impact on the accuracy of the measurements was not taken into account in (9)–(12).

3.1.3. The model of the charge exchange-spectrum of beam neutral. The emissivity of the D_α line at a point due to charge exchange reactions of the beam hydrogen atoms with deuterium ions of plasma was calculated as follows:

$$\varepsilon_{32}^{(CX)} = \frac{1}{4\pi} n_{D_+} n_H^{(Beam)} \frac{1}{\sum_{n'} P_{n'}} \times \sum_n P_n(\epsilon_{int}) q_{32_n}^{(CX)}(\epsilon_{int}, n_{D_+}, T_{D_+}, Z_{eff}), \quad (13)$$

$$P_n(\epsilon_{int}) = \frac{1}{n_e} \sum_{i=1}^{m} Z_i n_i P_n^{(i)}\left(\epsilon_{int}, n_{e,i}^{(eq)}, T_i\right), \quad (14)$$

where P_n is the population of the nth excited state of the beam atoms ($n = 1$ corresponds to the ground state), $P_n^{(i)}$ is the population of the nth excited state due to interaction with the ions of the ith type and the corresponding fraction of electrons, $q_{32_n}^{(CX)}$ is the coefficient of photon emission of the D_α line due to charge exchange reactions of beam atoms in the nth excited state with deuterium ions, Z_{eff} is the effective plasma charge, n_{D_+} is the density of the deuterium ions, and T_{D_+} is the temperature of deuterium ions. The values of $P_n^{(i)}$ and $q_{32_n}^{(CX)}$ were adapted from the ADAS database.

The Zeeman splitting is usually neglected upon calculation of the charge-exchange spectrum, because it is barely visible in the background of strong Doppler broadening (the charge-exchange neutrals have the temperature of plasma ions). However, it can be noticeable in the magnetic field with a magnitude of 8 T planned for the TRT. The spectral distribution of intensity was calculated using the model of the parameterized Zeeman triplet [13] that emulates the Paschen–Back effect but with corrections for the fine structure of levels:

$$f_{32}^{(CX)}(\lambda) = \left(\frac{\sin^2(\vartheta)}{4} + \frac{\cos^2(\vartheta)}{2}\right) \times \left(f_G(\lambda_{\sigma_+}, \sigma_G) + f_G(\lambda_{\sigma_-}, \sigma_G)\right) + \frac{\sin^2(\vartheta)}{2} f_G(\lambda_\pi, \sigma_G), \quad (15)$$

$$\lambda_\pi = \lambda_{32}(1 + \mathbf{v}_{\mathbf{D}_+}\mathbf{l}/c), \quad \lambda_{\sigma_\pm} = \left(\lambda_{32} \pm \frac{\alpha}{2} B\right)(1 + \mathbf{v}_{\mathbf{D}_+}\mathbf{l}/c), \quad (16)$$

$$\sigma_G = \lambda_{32}\sqrt{\frac{T_{D_+}}{m_D c^2}}\left(1 + \beta^2 T_{D_+}^{2\gamma}\right), \quad (17)$$

where ϑ is the angle between the direction of magnetic field **B** and the line of sight, $\mathbf{v}_{\mathbf{D}+}$ is the average velocity of deuterium ions at a given point, while α, β, and γ are the numerical parameters adapted from [13].

3.1.4. The model of the passive emission of the D_α line. Emissivity of the D_α line at a point due to the electron-impact excitation of neutral atoms from plasma and recombination of plasma ions is calculated using the following expression:

$$\varepsilon_{32}^{(Plasma)} = \frac{1}{4\pi} n_D n_e q_{32}^{(exc)}(n_e, T_e) + \frac{1}{4\pi} n_{D_+} n_e q_{32}^{(rec)}(n_e, T_e), \quad (18)$$

where n_D is the density of deuterium atoms in plasma; n_e and T_e are the electron density and temperature, respectively; $q_{32}^{(exc)}$ and $q_{32}^{(rec)}$ are the coefficients of photon emission upon electron-impact excitation and recombination, respectively.

Passive emission of the D_α line from the Scrap-Off Layer (SOL) crossed by the lines of sight, along with the light reflected from the metal walls of the tokamak vessel, including the light emitted in the divertor, will be visible along the MSE line of sight. Calculations carried out using the Scrap-Off Layer Plasma Simulation (SOLPS) code [14] revealed that the electron density in the divertor can exceed 10^{21} m^{-3}, which, in combination with the relatively low electron temperature of ~1–10 eV, leads to the necessity of taking into account not only the Doppler broadening but also the Stark broadening of the D_α line.

To take into account the Doppler and Stark broadening of the hydrogen-isotope spectral line simultaneously in the case of their Maxwellian distribution, the

following convolution has to be calculated at each point in space:

$$V\left(\lambda-\lambda_0,\Delta\lambda_{1/2}^{(G)},\Delta\lambda_{1/2}^{(L)}\right) = \int_{-\infty}^{\infty} G\left(\lambda'-\lambda_0,\Delta\lambda_{1/2}^{(G)}\right) L\left(\lambda-\lambda'-\lambda_0,\Delta\lambda_{1/2}^{(L)}\right) d\lambda', \quad (19)$$

$$L\left(\lambda,\Delta\lambda_{1/2}^{(L)}\right) = \frac{C_0\left(\Delta\lambda_{1/2}^{(L)}\right)^{3/2}}{\lambda^{5/2}+\left(\frac{\Delta\lambda_{1/2}^{(L)}}{2}\right)^{5/2}}, \quad (20)$$

$$\Delta\lambda_{1/2}^{(L)} = C_{ij}\frac{n_e^{a_{ij}}}{T_e^{b_{ij}}}, \quad (21)$$

where $C_0\left(\lambda,\Delta\lambda_{1/2}^{(G)}\right)$ is the Gaussian distribution; $L_0\left(\lambda,\Delta\lambda_{1/2}^{(L)}\right)$ is the Lorentz distribution but with an exponent of 5/2 instead of 2 (see [15]); $\Delta\lambda_{1/2}^{(G)}$ and $\Delta\lambda_{1/2}^{(L)}$ are the half-widths of the Gaussian and Lorentz distributions, respectively; a_{ij}, b_{ij}, and C_{ij} are the parameters adapted from [15]; C_0 is the normalization constant; λ_0 is the wavelength corresponding to the line center taking into account the Doppler shift due to the non-zero projection of the particle average velocity on the line of sight. Distribution (19) is known as the Voigt distribution.

To speed up integration along the rays upon ray tracing simulation, exact relation (19) was replaced by the so-called pseudo-Voigt distribution [16] of the form

$$V_p\left(\lambda-\lambda_0,\Delta\lambda_{1/2}^{(G)},\Delta\lambda_{1/2}^{(L)}\right) = \eta L\left(\lambda-\lambda_0,\Delta\lambda_{1/2}^{(V)}\right)+(1-\eta)G\left(\lambda-\lambda_0,\Delta\lambda_{1/2}^{(V)}\right), \quad (22)$$

$$\Delta\lambda_{1/2}^{(V)} \equiv F\left(\Delta\lambda_{1/2}^{(G)},\Delta\lambda_{1/2}^{(L)}\right), \quad (23)$$

$$\eta \equiv f\left(\Delta\lambda_{1/2}^{(G)},\Delta\lambda_{1/2}^{(L)}\right), \quad (24)$$

where $\Delta\lambda_{1/2}^{(V)}$, the half-width of the Voigt distribution, and η, the weight of the Lorentz distribution in the pseudo-Voigt distribution, are functions of $\Delta\lambda_{1/2}^{(G)}$ and $\Delta\lambda_{1/2}^{(L)}$.

Factor F can be approximated by the sixth-order polynomials of $x=\Delta\lambda_{1/2}^{(G)}/\Delta\lambda_{1/2}^{(L)}$ at $\Delta\lambda_{1/2}^{(G)}/\Delta\lambda_{1/2}^{(L)}\le 1$ and $x=\Delta\lambda_{1/2}^{(L)}/\Delta\lambda_{1/2}^{(G)}$ at $\Delta\lambda_{1/2}^{(G)}/\Delta\lambda_{1/2}^{(L)}\ge 1$:

$$\Delta\lambda_{1/2}^{(V)} \approx \begin{cases} \Delta\lambda_{1/2}^{(L)}\left(1+\sum_{n=1}^{6}a_n\left(\frac{\Delta\lambda_{1/2}^{(G)}}{\Delta\lambda_{1/2}^{(L)}}\right)^n\right), & \Delta\lambda_{1/2}^{(G)}/\Delta\lambda_{1/2}^{(L)}\le 1 \\ \Delta\lambda_{1/2}^{(G)}\left(1+\sum_{n=1}^{6}b_n\left(\frac{\Delta\lambda_{1/2}^{(L)}}{\Delta\lambda_{1/2}^{(G)}}\right)^n\right), & \Delta\lambda_{1/2}^{(L)}/\Delta\lambda_{1/2}^{(G)}\le 1 \end{cases}. \quad (25)$$

Weight factor η can be approximated by the logarithmic fifth-order polynomial the coefficients of which are found by fitting (19) by function (22):

$$\eta = \exp\left(\sum_{n=0}^{5}c_n\left(ln\left(\frac{\Delta\lambda_{1/2}^{(L)}}{\Delta\lambda_{1/2}^{(V)}}\right)\right)^n\right). \quad (26)$$

The relative difference of the pseudo-Voigt and Voigt distributions at $\lambda-\lambda_0\sim 2\Delta\lambda_{1/2}^{(V)}$ can reach 20%, but the main characteristics of the Voigt distribution, namely, its amplitude at maximum, half-width, and decay in the tail of the spectral line shape are reproduced correctly.

The Zeeman splitting was added into the Doppler–Stark model approximately, similar to [15], i.e., the Stark–Doppler line broadening was calculated for each Zeeman component.

3.1.5. The model of the bremsstrahlung radiation. The spectral emissivity of the bremsstrahlung radiation was calculated using the well-known expression (5.3.40) from [17]:

$$\varepsilon_{\text{Brems}}(\lambda) = \left(\frac{e^2}{4\pi\epsilon_0}\right)^3\frac{32\pi^2}{3\sqrt{3}m_e^2c^3}\sqrt{\frac{2m_e}{\pi e}}\frac{c}{4\pi\lambda^2}n_e\sqrt{T_e} \times \exp\left(-hc/\lambda T_e\right)\sum_{i=1}^{m}g_{\text{ff}}\left(Z_i,T_e,\lambda\right)n_iZ_i^2, \quad (27)$$

where ϵ_0 is the dielectric permittivity of vacuum, and g_{ff} is the Gaunt factor for the free–free transitions. The tabulated values of the latter factor were adapted from [18]. They differ from the values found in [19] only by an extended range of parameters for which they were calculated.

3.2. Initial Data Used in the Simulation

Plasma profiles obtained by combining the one-dimensional profiles for the core region calculated using the Automated System for Transport Analysis (ASTRA) code [20] that were published in [21] with

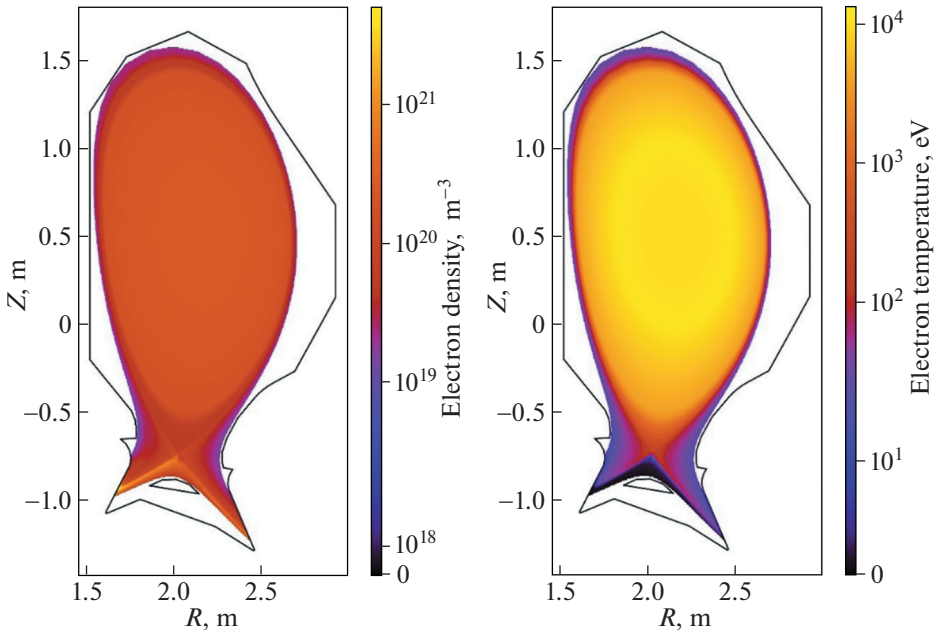

Fig. 2. Poloidal distributions of the electron density and temperature used in the simulations.

the two-dimensional distributions in the SOL calculated by means of the SOLPS code were used in the calculations. Parameters of deuterium plasma with an admixture of neon in the scenario with heat flux through the separatrix equal to 20 MW (which corresponds to auxiliary-plasma-heating power of 28.5 MW), average electron density at the separatrix of 7.8×10^{19} m^{-3}, and average electron and ion temperatures at the separatrix of 160 and 260 eV, respectively, were calculated with the SOLPS. The profiles of the electron density and temperature in the calculated scenario are presented in Fig. 2, while the profiles of the effective plasma charge and passive radiance of the D_α line calculated using Eq. (18) are presented in Fig. 3.

To take into account reflections from the plasma facing elements, we used a three-dimensional solid-state model of the tokamak (i.e., the analytically specified model rather than the polygonal one) presented in Fig. 4. The model was divided into three parts: the vacuum vessel with flanges, the first wall, and the divertor. The surface of the first wall was assumed to be fabricated from beryllium, that of the divertor was assumed to be fabricated from tungsten, and the vacuum vessel was assumed to be fabricated from steel. The Cook–Torrance model [22] with microfaces and the roughness parameters varying from 0 (mirror reflection) to 1 (diffuse reflection) was used as the model of the bidirectional reflectance distribution function. The roughness parameter was chosen equal to 0.26 for beryllium, 0.29 for tungsten, and 0.13 for steel. The same model of reflectivity (with the same values of the roughness parameter) was used in [23] for the JET-ILW and in [24] for the ITER tokamak.

Simulation in the present work was carried out for hydrogen diagnostic beam. The initial data for its description in the Cherab code are energy E_0 of the fast beam neutrals, standard deviation of the beam in focus σ, angles α_x and α_y of beam divergence, along with the total concentration of the beam atoms and position of its focus. For circular beam cross section, we assumed that $\alpha_x = \alpha_y$. Position of focus was fixed at the magnetic axis of the plasma column. To define the beam parameters, we assumed that the ion-optical system of the diagnostic injector formed an ion beam with a current of $I = 15$ A. The emission current density was set equal to 120 mA/cm^2. The local angular divergence α of the formed beam and its radius r at the focus were determined in the course of calculations of an individual cell of the ion-optical system by means of the PBGUNs software. The calculation results are presented in Fig. 5.

We also took into account that the beam formed by the ion source of the diagnostic injector contained molecular ions H_2^+ and H_3^+ in addition to protons H^+. Atoms with energies of $E_0/2$ and $E_0/3$ are formed, respectively, from these molecular ions upon ion-beam neutralization. The equivalent current of atoms of each component I_{eq} after charge exchange was calculated using expression

$$I_{eq}(E_i) = m_i P_i F_i I, \tag{28}$$

where F_i is the efficiency of charge exchange of the ith component [25], P_i is its fraction in the beam composition, and m_i is its atomic weight. The composition of

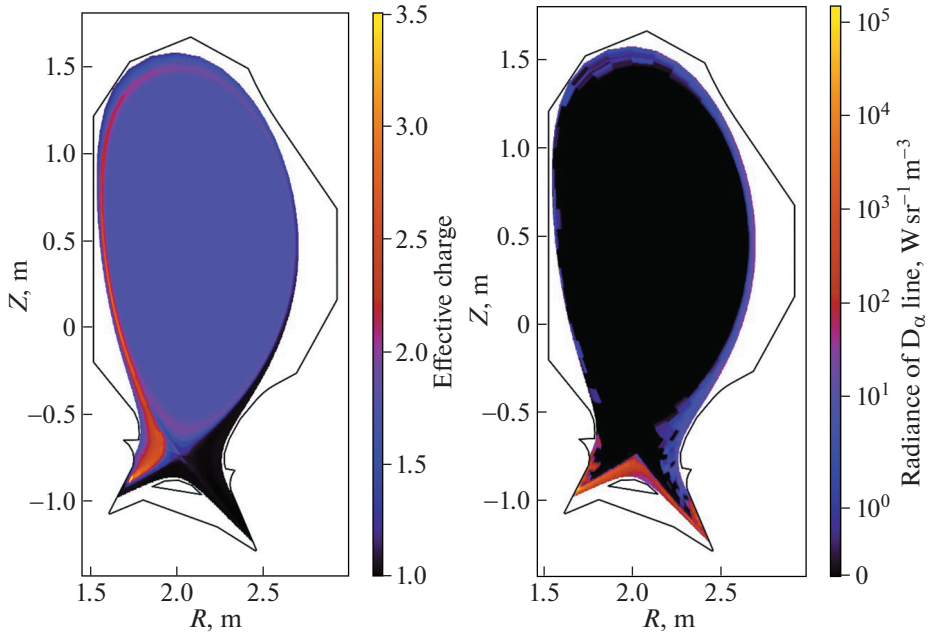

Fig. 3. Poloidal distributions of the effective plasma charge and passive radiance at the D_α line used in the simulations.

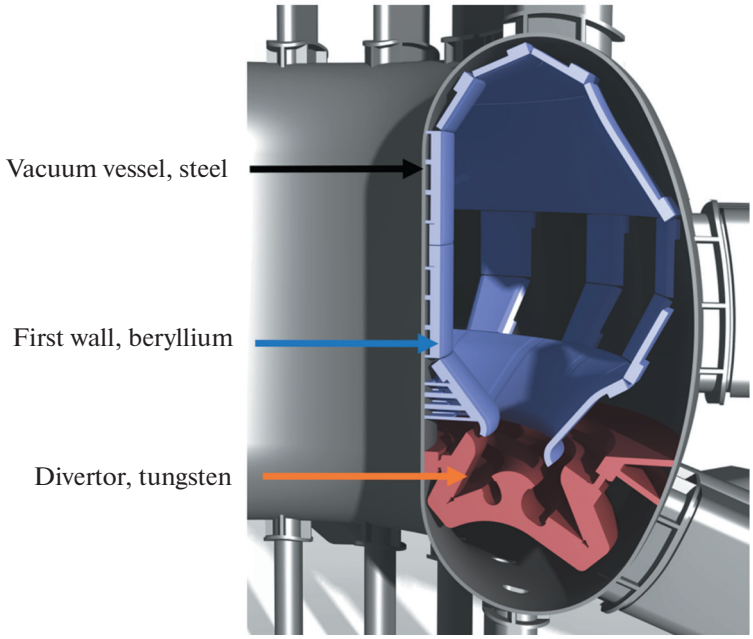

Fig. 4. Cross section of the 3D model of the TRT vessel used in the simulations.

the ion beam was assumed to be the same as in [26]: $H^+ : H_2^+ : H_3^+ = 0.85 : 0.05 : 0.10$.

3.3. Composition of the Model Spectrum

Application of the described models to objects of the TRT tokamak vessel, plasma, and beam allowed performing calculations of the passive and active plasma emission spectra. The following components were taken into account: bremsstrahlung (27), passive D_α line of plasma (18)–(26), along with the active spectra of beam emission (8)–(12) and charge exchange of plasma ions with beam atoms (13)–(17). It should be noted that we did not take into account

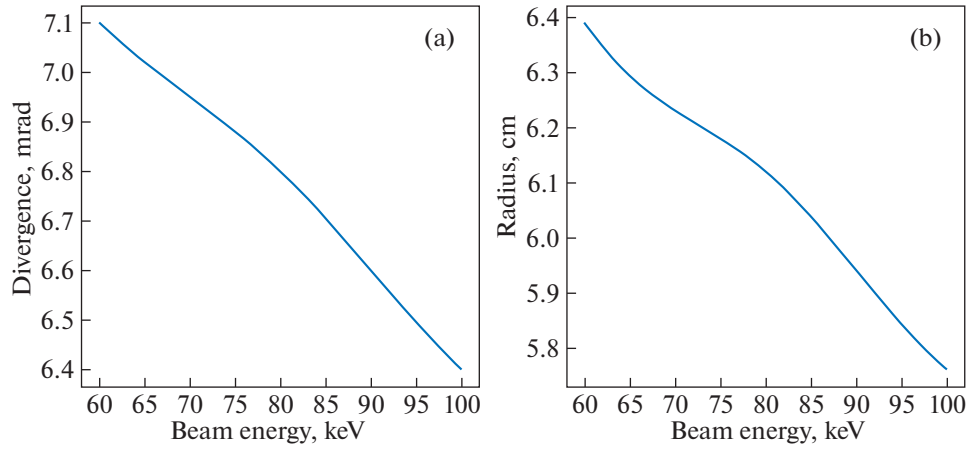

Fig. 5. Parameters of the diagnostic beam as a function of its energy.

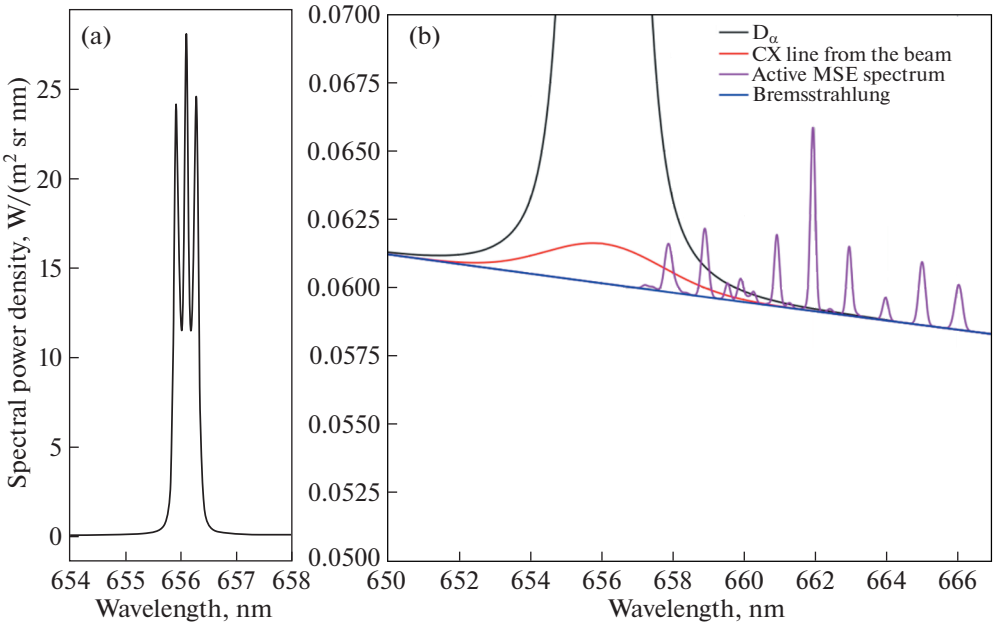

Fig. 6. General view of the simulated spectrum obtained along the line of sight starting from the equatorial port in the cross section adjacent to the DNB and directed to the crossing point of the beam and the plasma-column center (left), along with its composition (right).

the emission of the lines of plasma impurity ions in the model spectrum. In particular, we did not take into account the contribution of the C II multiplet that is capable of partial overlapping with the MSE spectrum, as was demonstrated in [27], since the SOLPS simulation was performed for the TRT tokamak without taking into account the carbon impurity. An example of the simulated spectrum is presented in Fig. 6. The passive plasma line D_α the main contribution to which is associated with radiation coming from the divertor and appearing at the line of sight as a result of reflections from the first wall is shown on the left-hand side, while part of the spectrum on a larger scale is presented on the right-hand side in the background of the passive-line wing. All considered spectral components can be seen: the passive line of plasma, the bremsstrahlung continuum, the active charge-exchange line of the beam, and the active MSE spectrum of the beam. The active spectrum in the background of the D_α line is shown in detail in Fig. 7. Contributions of each of the three energy components of the diagnostic beam to the total active spectrum are shown separately. The spectra presented in Figs. 6 and 7 were calculated for the line of sight starting from the

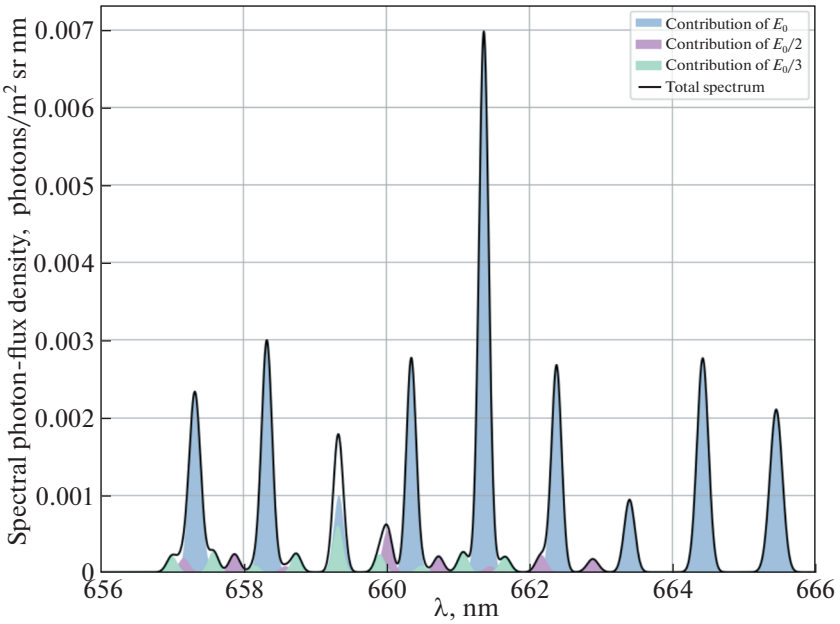

Fig. 7. Contribution of individual components of the diagnostic beam to the MSE spectrum for the central line of sight.

equatorial port in the cross section adjacent to the diagnostic injector and directed to the crossing point of the beam and the magnetic axis of the plasma column.

The simulation was carried out in two stages: the preliminary calculation aimed at determining parameters of the light collection system, along with parameters of the diagnostic injector, and the more detailed calculation aimed at estimating the requirements for the spectral device and the detector. The preliminary calculation was performed in the approximation of infinitely thin lines of sight, and reflections from the vessel walls were taken into account only for the passive components of the spectrum. Such an approximation did not affect position of the peaks of the spectral lines, which allowed estimating the dependence of the relative position of the active MSE signal and the background on the direction of observation and parameters of the diagnostic injector. At the second stage, we specified the size and numerical aperture of the fiber-optic collector, along with optics in front of it that focuses the cone of light collected from the center of the diagnostic beam. The following factors were also taken into account: the influence of optics and the spectral device on the obtained spectrum, along with the statistical noise.

4. LIGHT COLLECTION SYSTEM FOR THE MSE DIAGNOSTIC

The shape and position of the MSE spectrum relative to the background components will be determined by position of the light collection system with respect to the axis of injection of fast atoms. To determine characteristics of the light collection system for the MSE diagnostic, it is necessary to determine in which diagnostic port it will be located. In the present work, we analyzed the variants of location that allow observation of the diagnostic beam injected radially in the equatorial plane of the tokamak. Under the conditions of the planned TRT geometry, we considered locating the light-collection system in the diagnostic ports located in four cross sections adjacent to the beam. The vertical ports in the injection cross section were not taken into consideration at this stage since the angle between the lines of sight in the central region of the plasma column and the diagnostic beam would be close to 90°. Such observation geometry would not allow shifting the active MSE spectrum relative to the passive D_α line due to the Doppler effect. The equatorial ports also allow mounting a larger number of optical devices, adjustment systems, shutters, and other necessary elements of the light collection systems.

4.1. The Choice of the Observation Position for Detecting the Signal along the Central Line of Sight

The variants of observation of the central part of the plasma column analyzed in the present work are illustrated in Fig. 8 that presents the plane of the magnetic axis of the plasma column. The observation points were arranged in the center of the equatorial ports as close to plasma as possible but beyond the first wall on the circle of radius $R = 3$ m. Such a distance allows placing a mirror in front of the observation point that is necessary for protecting optics from the direct flux of plasma neutrons. The influence of this mirror on the signal for the MSE-LS diagnostic can be

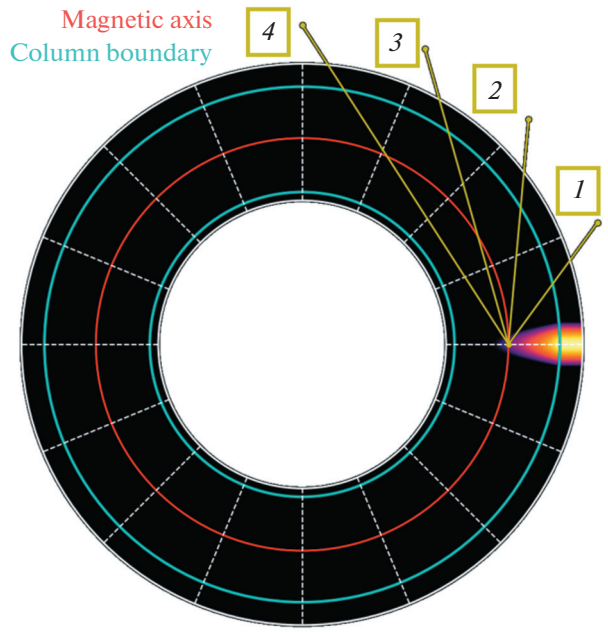

Fig. 8. Possible variants of observation of the central area of the plasma column.

taken into account in the overall transmission coefficient of the light collection system. For the fifth cross section relative to the beam, despite it providing adequate conditions for observation, part of the lines of sight (observing the center of the plasma column) pass the high-field side (HFS) SOL, which substantially increases the level of passive signal collected along these lines of sight and reduces the ratio of the useful signal to the total one. Therefore, this cross section was also excluded from analysis.

For the four selected variants, we carried out simulation of the active spectrum and determined its total intensity as a function of the diagnostic beam energy. The results of the simulation are presented in Fig. 9a. It can be seen that the lines of sight from the first and fourth cross sections allow collecting considerably higher radiation intensities upon observation of the central region of the plasma column than observation along the other two lines of sight. In addition, the same two cross sections allow obtaining a larger shift of the active spectrum relative to the passive D_α line due to more shallow angles between the direction of observation and the direction of beam injection, which is illustrated in Fig. 9b. Figure 9 also allows to conclude that higher beam energy is preferable for the MSE measurements: the transition from 60 to 100 keV increases the integral useful signal by 60% and provides a 1–1.5-nm larger shift for the central lines of sight. Based on these results, it is suggested to consider only two variants of arrangement of the light collection systems for the MSE-LS diagnostic, namely, those in cross sections 1 (LOS 1) and 4 (LOS 4).

The difference between these two lines of sight consists in the fact that the projection of the beam direction on the line-of-sight direction for line of sight 1 is positive, and the active signal will experience the red shift, while the same projection for the line of sight 4 is negative, and the active signal will experience the blue shift. The optimal shift direction will be determined by the composition of plasma impurities. The absence of strong spectral lines of impurities on one of the sides of the passive D_α line will facilitate isolation of the active signal and processing of the spectrum.

From the point of view of observation angles, the difference between lines of sight 1 and 4 consists in the fact that, for the cross section adjacent to the beam,

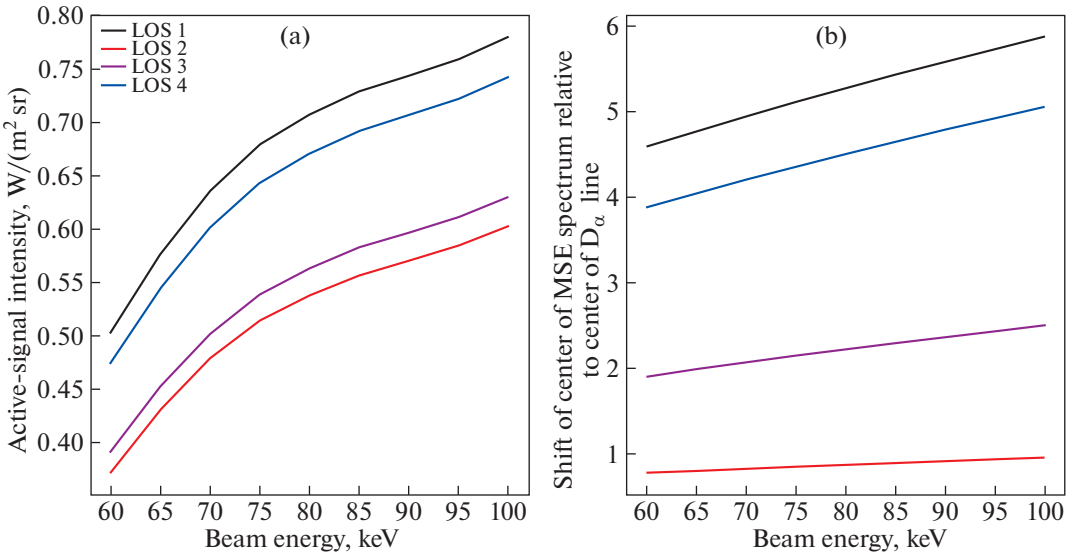

Fig. 9. Integral characteristics of the MSE signals for possible variants of observation.

the lines of sight directed to the center of the plasma column provide larger shift of the active spectrum than the peripheral ones. For the observation from cross section 4, the situation is opposite: the active spectrum shifts more for the peripheral lines of sight than for the central ones. In this regard, when arranging the system of measurements, it could be advantageous to separate the light collection systems with respect to areas of observation into two, the central and the peripheral ones, and mounting them in different diagnostic ports. On the one hand, this would lower the requirements for the light collection optics, but, on the other hand, would increase their number.

4.2. Parameters of the Light Collection System

In order to determine parameters of the light collection systems, we carried out simulation of the active and passive spectra obtained for five lines of sight for two selected observation points. The lines of sight were directed to different points located on the minor plasma radius between $\rho = 0$ and $\rho = 1$ on the low-field side where concentration of the beam atoms is the highest. The geometry of the lines of sight specified in the simulations is illustrated in Fig. 10. The dependence of the total intensity of the active signal on the diagnostic beam-injector energy was obtained for each line of sight. The results of simulation for LOS 1 in absolute units are presented in Fig. 11b while those normalized to maximum value for each line of sight are presented in Fig. 11a. It is evident from Fig. 11b that for the core plasma, the highest intensity is achieved at energy of the main component equal to 100 keV, while that for the peripheral area is achieved at 60 keV. The total brightness of the signal obtained by the peripheral lines of sight, however, drops by 30% upon transition from low beam energies to high ones. It can be seen from Fig. 11a that the intensity obtained by the peripheral lines of sight exceeds that obtained along the central lines of sight by a factor of 10–15 in entire range of studied energies. This is also true for LOS 4.

One of the main characteristics of a photographic lens is its f-number that determines its etendue. Since the active-signal intensity in the central area is low, f-number should be as small as possible. In the process, the total etendue of the diagnostic will be determined by the component with the lowest etendue. This is usually the spectrometer, the most expensive and complex device. For spectrometers used for the MSE diagnostic in tokamaks, the lenses with f-numbers of <F/4.0 are used most widely [28, 29]. The devices characterized by f-numbers of F/2.5–F/3.5 are used as well [30]. The brightest of the spectroscopic instruments is close to F/2.0 [31, 32]. At the present stage of development of the MSE diagnostic, it is suggested using optics with an f-number of F/3.0.

The viewing angles for each of the proposed variants of the light-collection-system arrangement are

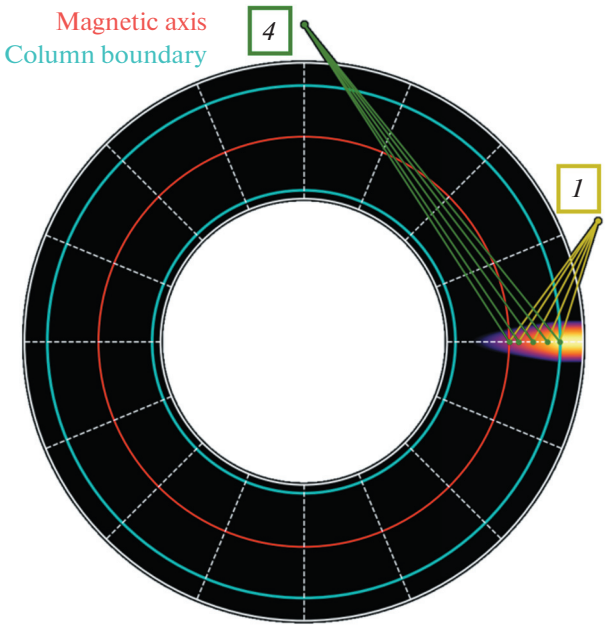

Fig. 10. Geometry of observation of entire plasma-column radius for chosen points of observation.

presented in Fig. 12. For the integrated system located in port 1 (Fig. 12a), a lens with a viewing angle starting from 26° is needed, provided that the optical axis is directed at $\rho = 0.5$. It should be considered that the light-collection efficiency reduces substantially at large divergences from the optical axis of the lens due to vignetting. Therefore, in the case of such a position of the optical axis, designing lenses with large collection angles and suppressed vignetting would be optimal. If, however, vignetting of the lens cannot be suppressed to the desired level, the optical axis of the collection system should be shifted closer to the plasma column center, because the amount of light emitted in this area is an order of magnitude lower than at the plasma edge, and usable surface area of the lens should be maximized. When the optical axis of the light-collection system crosses the beam at $\rho = 0.2$, the viewing angle for detection of radiation over entire range of values of minor radius equals to 37°, while that for the crossing point located at $\rho = 0$ equals to 52°.

The effective focal length of the lens for the LOS 1 system can be determined from the main equation of geometric optics: $f = a/(m + 1)$, where a is the object range and m is the image reduction by the lens. The object range is determined by position of the collection system. The compression is limited from below by the size of the port in which the image of the diagnostic beam will be formed by the lens and limited from above by the required spatial resolution for given input diameter of the optical fiber. For minimum distance from the first mirror to the image inside the port, the scale will be limited at the level of $m \approx 5$ by the pipe

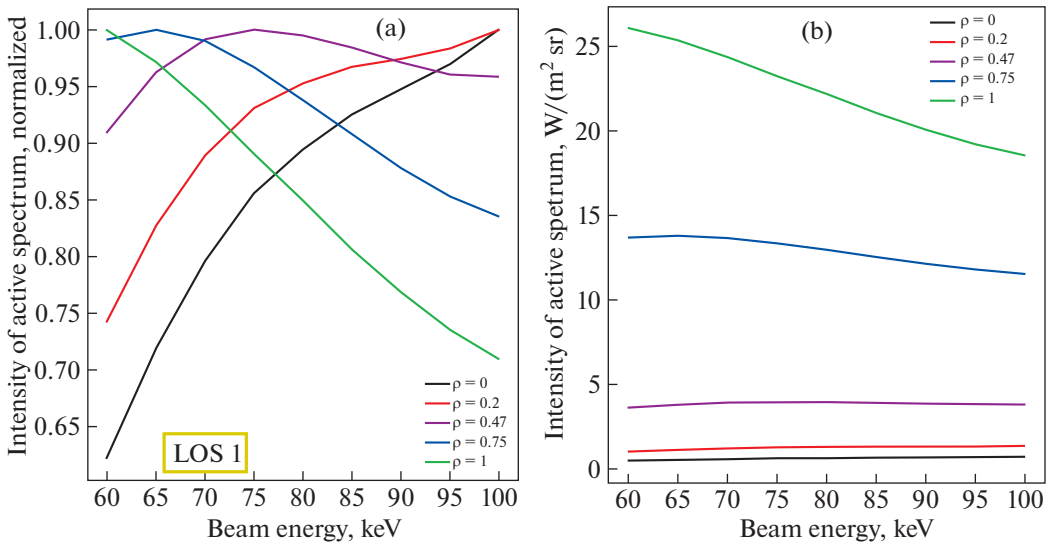

Fig. 11. Intensity of the MSE signal as a function of the diagnostic-beam energy.

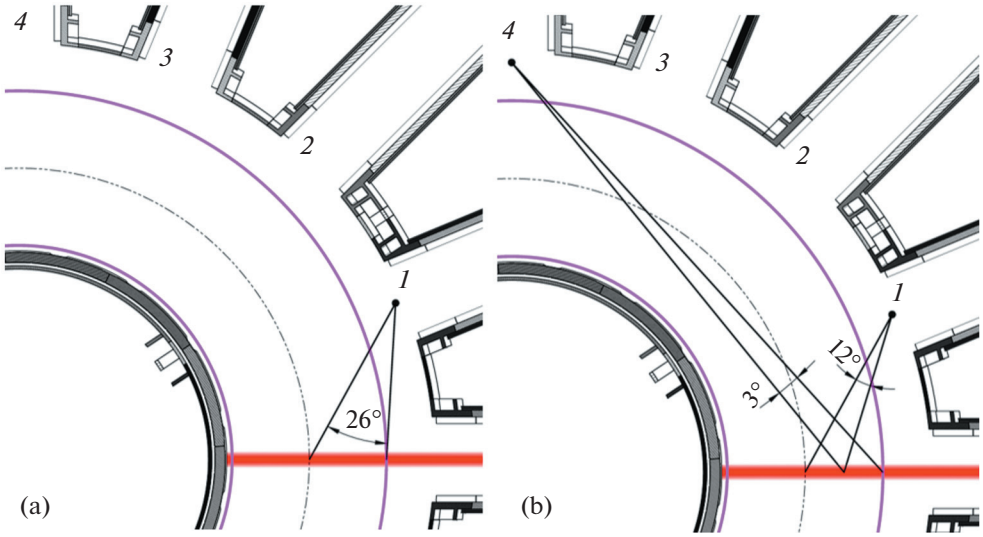

Fig. 12. Visual angles for LOS 1 and LOS 4.

geometry: the collection system has to be fitted into it, and a space of about 15–25 cm should be left behind the optical-fiber holder for convenience of its installation and exploitation. In this case, the effective focal length will be equal to $f = a/(m + 1) = 1690/6 \approx 280$ mm for the central line of sight and $f = a/(m + 1) = 1460/6 \approx 240$ mm for the peripheral one. Under the condition that $f/D < 3.0$, the lens diameter should fall in the range of $D > 80$–90 mm. The image distance will fall in the range between 300 and 340 mm in this case.

Lenses with viewing angles of 12°–13° and 3°–4° in the 1 and 4 ports, respectively, will be sufficient for split light collection system to ensure overlap of their areas of observation (Fig. 12b). Image compression, the object range, etc. for the lens installed in cross section 1 remains the same. The image distance for the lens installed in cross section 4 is also specified based on considerations of the branch-pipe geometry and is limited by the necessity of light collection system adjustment and servicing. In this case, the distance to the beam will be on the order of 4–4.5 m, and the compression rate will be at the level of $m \approx 12$–15. For a fixed value of $m = 12$, the effective focal length of the lens and its diameter can be found using the line of sight directed along the optical axis: $f = a/(m + 1) = 4200/12 \approx 350$ mm, $D > 120$–140 mm.

Parameters of the lenses can be determined more precisely at later stages of system development since the collecting optics has to be integrated not only with the system of mirrors protecting it from the direct flux of neutrons but also with other diagnostic systems located in the same port. The design of the lenses must include correction for aberrations (chromatic and astigmatism) and vignetting in both variants of arrangement of the light collecting systems.

At the present stage of development, a multichannel fiber-optic collector with a numerical aperture that is at least as large as that of the collecting optics is planned to be used as the transmitting light guide for the MSE diagnostic. The number of channels will be determined by the size of the scientific-camera sensor and the rate of compression of the image projected onto the input slit of the spectral device. The fiber bundles for each line of sight are assembled into a solid square or rectangular assembly on the tokamak side while being arranged in a linear array on the spectral-device side.

The number of bundles in each channel can vary depending on the number of available spectrometers. From the tokamak side, the total number of bundles is limited by the size of the beam image formed by the lens. For the beam radius of 6 cm and the compression rate of 5 : 1, the radial dimension of the bundle assembly should not exceed 6 mm, while that for the scale of 12 : 1 should not be larger than 2.5 mm.

From the spectral-device side, the number of fiber bundles is limited by the size of the camera sensors available for this diagnostic. In other words, the number of fiber bundles that create a spot covering entire matrix of the scientific camera can be assembled for each line of sight. In this case, on the one hand, the number of spectrometers and cameras will increase, but, on the other hand, it will open the possibility of reducing the noise level thanks to binning. The other extreme case would be using a set of single-core optical fibers for each line of sight that, combined, create a spot matched to the size of the camera matrix. In this case, it is sufficient having only one spectral device, but intensity of the signal detected by the sensor will be lower. In any case, the ratio of the active signal to the total one weakly depends on the number of bundles. Therefore, the possibility of using a single-core optical fiber with core diameter of 400 μm was considered at the present stage.

5. PARAMETERS OF THE DIAGNOSTIC INJECTOR OF FAST ATOMS

The diagnostic injector for the MSE-LS technique represents the most technically complex and critically important element since its parameters determine the principal possibility of conducting measurements, along with the ultimate accuracy and spatiotemporal resolution of the measured quantities. Therefore, simulation of the active signal for various variants of diagnostic injector design is an important stage of the MSE-diagnostic development for the TRT tokamak.

5.1. The Influence of Energy of the Main Component on the Possibility of Carrying out the MSE Measurements

When solving the problem under consideration using the Cherab code according to the model described by Eqs. (3)–(6) and (28), we specified that the diagnostic beam has energy E_0 of the main component in the range from 60 to 100 keV, which corresponds to the energies of the diagnostic beams widely used at other facilities [26, 33]. First of all, it is worth noting the influence of this parameter on the current of the beam atoms at the output of the diagnostic injector that is described by Eq. (28) and illustrated in Fig. 13. It is evident from the figure that the total current drops by ≈35% with increase in the main-component energy. The component composition of the beam changes considerably due to reduction in the neutralization efficiency of the hydrogen ions. Starting from the energy of 86 keV, the component with energy of $E_0/3$ represents the major part of the beam current. This fact can have a negative impact on the composition of the active spectrum generated by the beam. The contribution of each of the beam components to the active MSE spectrum at plasma periphery (LOS 1, $\rho = 1$, $E_0 = 100$ keV) is illustrated in Fig. 14. It can be seen that the brightest line in the spectrum is emitted by particles with energy of $E_0/3$, and most lines overlap with each other. Processing such a spectrum is diffi-

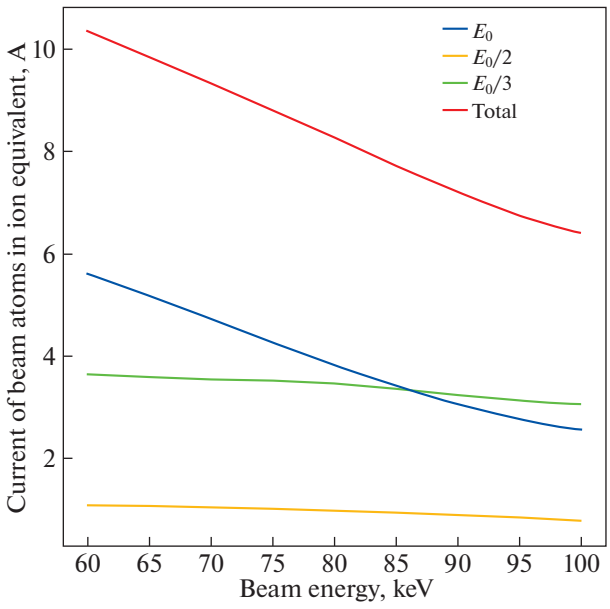

Fig. 13. Current of beam atoms as a function of beam energy.

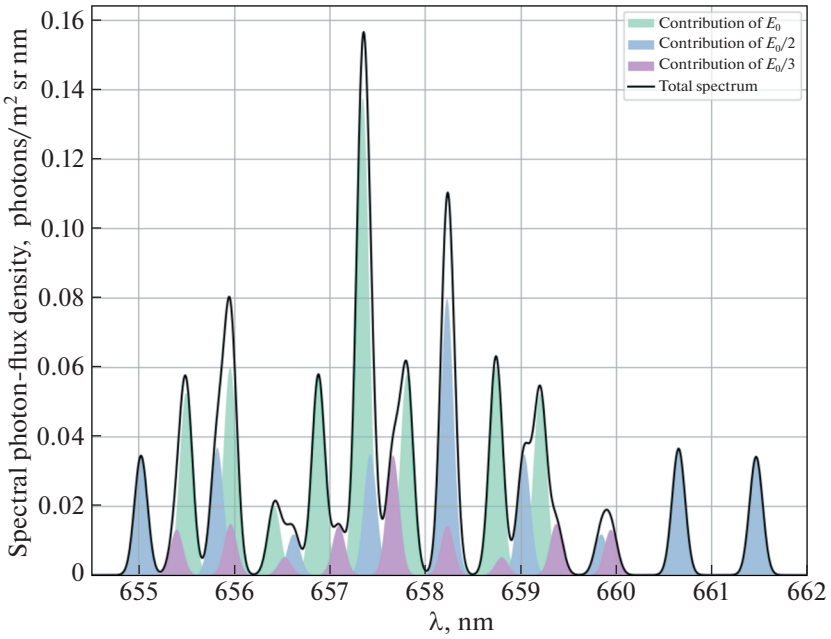

Fig. 14. Contribution of individual components of the diagnostic beam to the MSE spectrum for the peripheral line of sight.

cult and requires having accurate data on the beam parameters in a specific discharge. The beam energy, its component composition, and divergence must be known precisely. In this case, much less free parameters will remain upon solving the inverse problem for description of the experimental data: the Doppler shift of spectra of various beam components is predictable since it is independent of parameters of the tokamak plasma and magnetic field.

One line of sight crossing the injection axis in the inner volume of the injector is sufficient for controlling the main beam parameters. The spectra of the H_α line radiation of the beam recorded from it's vacuum vessel would allow obtaining information on the actual energy of the diagnostic beam, its component composition, and angular divergence in a specific pulse relatively straightforward. A port for such control of parameters should be provided in the design of the diagnostic injector, similar to, e.g., the DINA-KI60 injector [26].

The composition of the MSE spectrum would improve if the area of observation is shifted toward the center of plasma, and the contribution of the slow beam components nearly disappears at $\rho = 0$ (Fig. 7). This is because the beam components become weaker upon propagation through plasma. Penetration of the diagnostic beam into the TRT plasma at different energies was simulated using the Cherab code, and the results are presented in Fig. 15. It can be seen that losses of the injected atoms diminish at higher energy of the main component, and a larger fraction of the beam (by a factor of 2–3) reaches the central region of plasma. This occurs due to the reduction in the cross sections of interaction of the beam atoms with plasma with increase in energy of atoms.

In addition to spectral composition, the energy of the main component of the diagnostic beam strongly influences the Doppler shift of the active MSE spectrum. The spectrum shifts further away from the bright passive D_α line with increase in E_0 (Fig. 9b), which allows to lower the requirements for the detection system dynamic range. To obtain a quantitative estimate of the shift of the active spectrum, we introduced three parameters: width $\delta_{D\alpha}$ of the passive line, shift δ_π of the MSE spectrum (of the main component of the beam) with respect to the edge of the π-component, and shift δ_σ of the MSE spectrum with respect to the central line of the σ-component. These reference points are illustrated visually in Fig. 16. The ordinate axis in Fig. 16 coincides with the center of the D_α line. In this case, the fulfillment of condition $\delta_{D\alpha} \le \delta_\pi$ in any realization means that the active spectrum is shifted by the amount sufficient for preventing its overlap with the passive line of plasma emission, which greatly simplifies signal detection since intensity of the passive radiation reduces substantially. On the other hand, fulfillment of condition $\delta_{D\alpha} \le \delta_\sigma$ means that the active spectrum is shifted relative to the D_α line only half-way, so that only the distant triplet of the π-component and two lines of the central triplet of the σ-component (including the central one) do not overlap with the passive line. The second condition is less strict but still allows reconstructing the MSE spectrum based on the condition that intensities of the left and right halves of the spectrum are equal to each other.

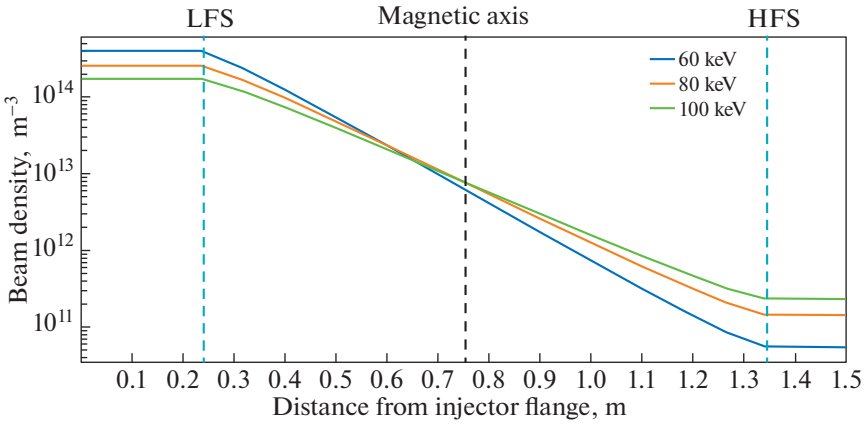

Fig. 15. Attenuation of the diagnostic beam of different energies upon propagation through plasma.

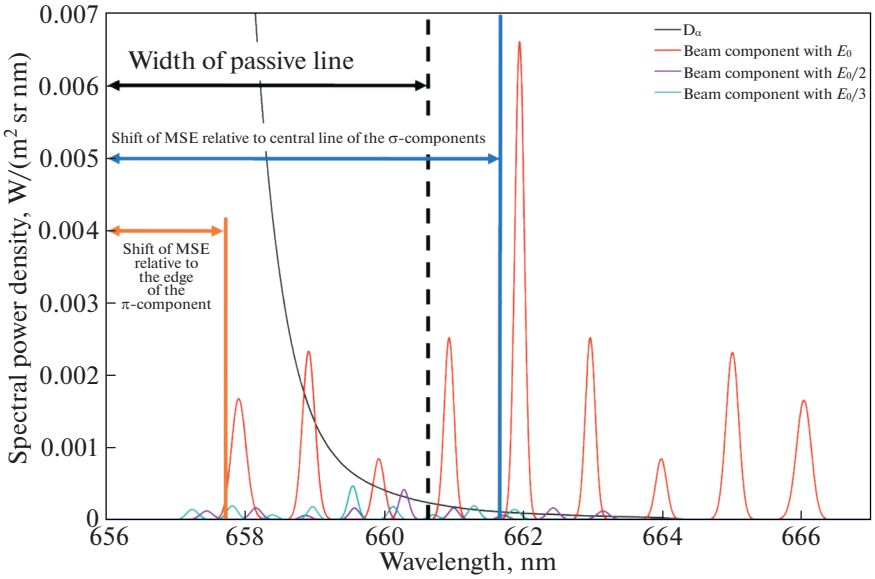

Fig. 16. Determination of position of the MSE spectrum relative to the passive plasma line.

The simulation revealed that the condition of $\delta_{D\alpha} \le \delta_\pi$ is not fulfilled for any of the chosen lines of sight, targeted regions, and energies of the main beam component. The results of calculation of $\delta_{D\alpha}$ and δ_σ are presented in Fig. 17. The values of $\delta_{D\alpha}$ for all lines of sight for both variants of collection-system arrangement are shown by the dashed lines, while the solid lines correspond to δ_σ. It is evident from Fig. 17a that the condition of $\delta_{D\alpha} \le \delta_\sigma$ is fulfilled for LOS 1 at $E_0 > 70$ keV, which means that the MSE measurements can be carried out. For the system of observation completely located in the 4th cross section relative to the injection cross section, this threshold is equal to 90 keV (Fig. 17b). For the partitioned system located in diagnostic ports 1 and 4, the same condition is fulfilled for all corresponding lines of sight at $E_0 > 70$ keV.

The energy of the main component of the diagnostic beam thus must be equal to or higher than 70 keV. However, the increasing dependence of intensity of the MSE signal on E_0 is indicative of the fact that higher beam energies (90–100 keV) could simplify the measurements of plasma parameters using the MSE-LS diagnostic.

5.2. Limitations on the Relative Position of the Diagnostic and Heating Injectors

A complex for auxiliary plasma heating that will include several heating injectors with energy of fast atoms of 250 or 500 keV is planned to be used in the TRT tokamak [34]. The tangential direction of their injection creates a relatively large area along the toroi-

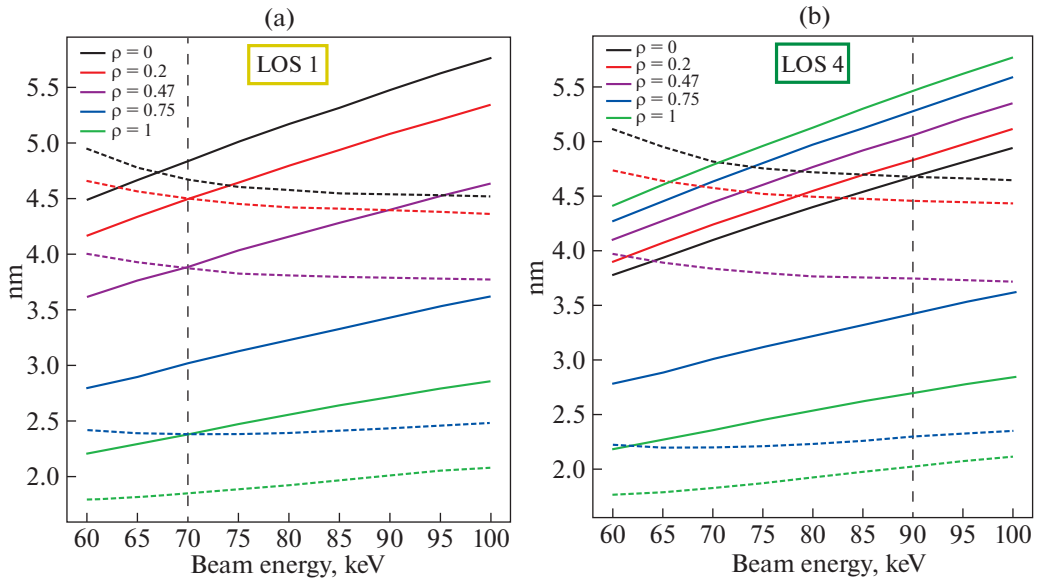

Fig. 17. Displacement of the MSE spectrum for the central line of the σ-component (solid lines) and the width of the background D_α line (dashed lines) for lines of sight 1 and 4 of the light collection systems.

dal loop of the column in which the lines of sight of the MSE diagnostic will cross heating beams. At several positions, the spectrum of radiation emitted by the heating beam will overlap with the MSE spectrum of the diagnostic beam. In order to avoid such a situation, we carried out combined simulation of emission of the diagnostic and heating beams for some of their relative positions. The model was specified according to the scheme depicted in Fig. 18. The diagnostic beam was injected radially in the center of the equatorial port in the plane of the magnetic axis of the plasma column. The diagnostic cross sections were numerated counterclockwise starting from the injection one. The heating beams were assumed to be injected into the chamber tangentially along the center of the tilted ports provided for this purpose in the sketches of the vacuum vessel. The fact that each heating injector contains two ion sources was taken into consideration. They were separated vertically and directed toward the magnetic axis of plasma as shown in Fig. 3 in [34]. The emission of radiation was simulated for the lines of sight of collection system LOS 1 and LOS 4. A set of spectra obtained for various relative positions of the heating and diagnostic beams was simulated. The heating beams were shifted from one cross section to the next by rotating them relative to the tokamak axis by 22.5° (the toroidal angle between the diagnostic cross sections).

As a result of simulation of spectra of the DNB and NBI radiation, we determined two variants of their spectral overlap:

(1) Overlap of the MSE spectrum of the diagnostic beam with the MSE spectrum of the heating beam;

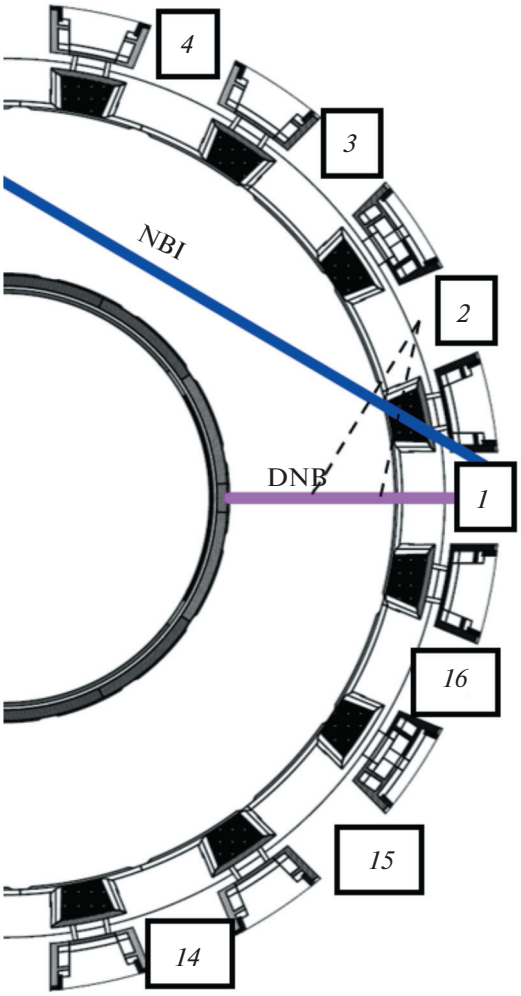

Fig. 18. Injection direction of the heating beam and numeration of the diagnostic cross sections.

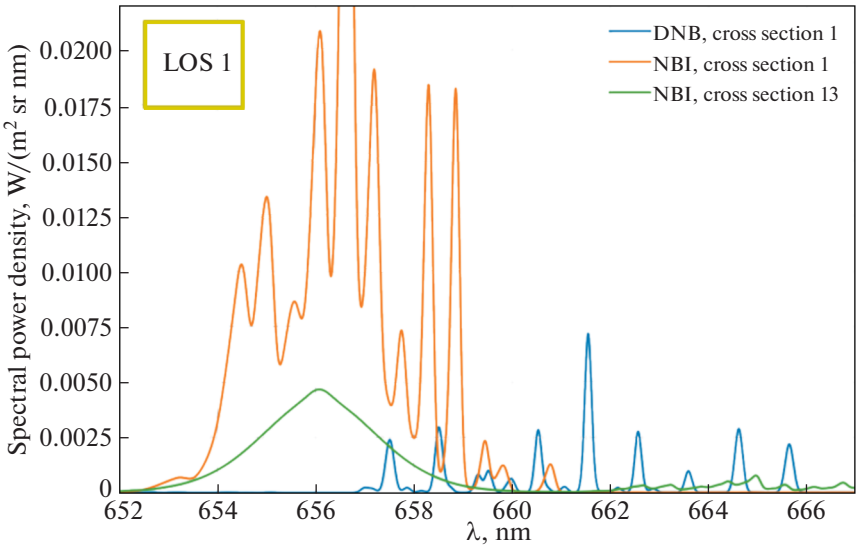

Fig. 19. Variants of overlap of the MSE spectrum from the diagnostic beam and the spectrum from the NBI.

(2) overlap of the MSE spectrum of the diagnostic beam with the D_α line emitted by plasma as a result of charge exchange with atoms of the heating beam (the CX spectrum).

The variants of position of the heating injector for which these situations take place are illustrated in Fig. 19. The total of two unwanted variants of the heating beam position relative to the diagnostic beam were found for the LOS 1 system: the spectra of the DNB and NBI overlap with each other in cross section 1, while the CX spectrum from the heating beam overlaps with the MSE spectrum in cross section 13. There were three unwanted cross sections for the LOS 4: the MSE and NBI spectra overlap in cross sections 3, 4, and 16. In addition, the CX spectrum from the NBI overlaps with the MSE spectrum in cross section 16.

Taking into account these data, we were able to formulate the following requirements for the diagnostic injector of fast atoms at the stage of the conceptual development of the MSE diagnostic:

(1) Energy of the main component of 90–100 keV;

(2) total current of beam atoms of 6.4–7.2 A;

(3) effective radius of 5.7–6.0 cm;

(4) positioning in the diagnostic port for which the DNB and NBI spectra do not overlap with each other.

6. THE MSE SIGNAL DETECTION SYSTEM

The MSE-signal detection system can be divided into two main parts:

(1) The spectrometer including an input slit, lenses, and a diffraction grating;

(2) the scientific camera.

To estimate the necessary parameters of the detection-system elements, we carried out simulation of light collection taking into account the influence of the line of sight and optics for collection system LOS 1 on the obtained spectrum. The collection system of light from plasma of the TRT tokamak is presented in Fig. 20. We specified a visual angle sufficient for entire collecting lens to be within the field of view instead of an infinitely thin line of sight. Position of the center of the collecting optics was specified in accordance with the previous stage of simulation, while position of the input face of the optical waveguide was adjusted in such a way that the chord was focused to the center of the diagnostic beam. The necessary position of the "pupil" was determined by means of the Raysect–LoggingRay functional. We also took into account

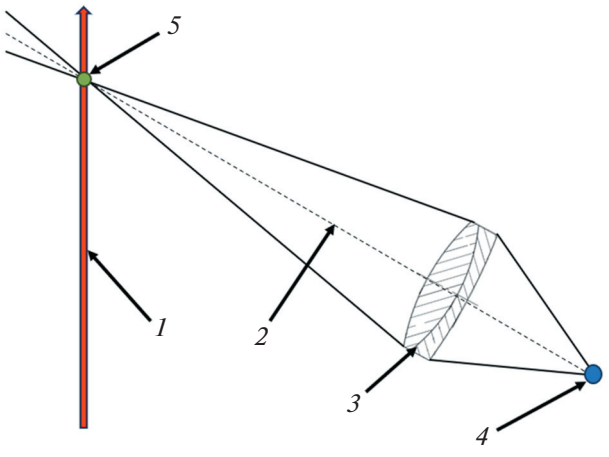

Fig. 20. The scheme of simulation of the spectrum taking into account the shape of the visual angle, collecting optics, and reflections.

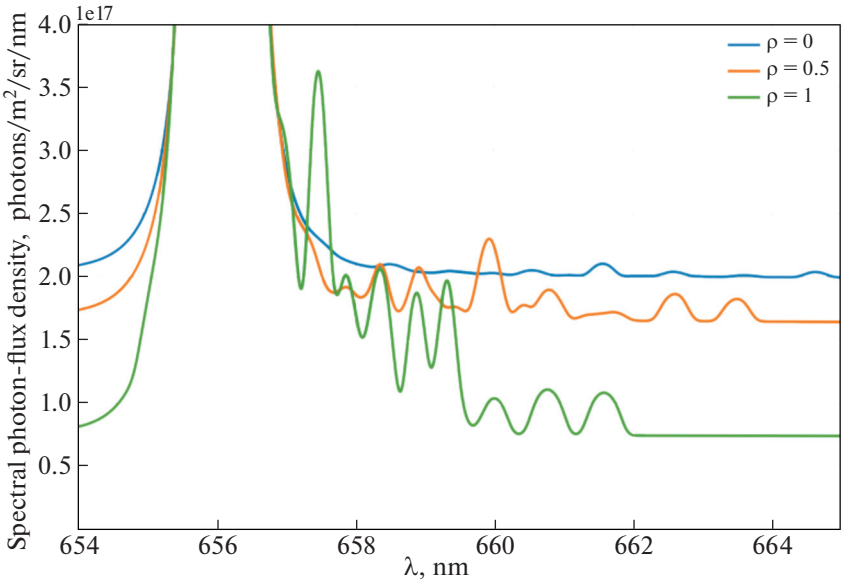

Fig. 21. Results of simulation of collection of light from plasma of the TRT tokamak.

reflections from the vessel walls for all spectral components.

A complex lens consisting of two lenses with a known optical design fabricated from materials chosen from the Raysect database was used as the collecting optics at the stage of the conceptual system development. Characteristics of lenses are listed in Table 1. When performing simulation for each chord, the complex lens was rotated so its optical axis coincided with the center of the observation chord in order to avoid spherical aberrations. In the scheme under consideration, simulation of light collection for LOS 1 was carried out for three observation chords directed to three plasma-column regions: $\rho = 0$, $\rho = 0.5$, and $\rho = 1$. The results of the simulation in the wavelength range of 654–665 nm are presented in Fig. 21. It can be seen that the magnitude of the passive signal for the central chord is a factor of ≈2.5 higher and that of the active signal is a factor of ≈25 lower relative to the chord directed to $\rho = 1$.

Following the simulation of light collection, the signal was processed taking into account the influence of the detection system. The obtained spectral power densities of radiation were converted to spectral densities of the photon flux. The obtained distributions were then convoluted with the instrumental function of the spectral device. At the present stage, a high-etendue, high-resolution spectrometer with a 200 groove/mm Echelette grating operating in high diffraction order (11–14) is intended to be used for the MSE diagnostic at the TRT facility. Its input lens has a focal length of 370 mm, and the output lens has the focal length of 260 mm. The spectrometer provides the dispersion of 5 Å/mm in the vicinity of the H_α line and the ultimate spectral resolution of 0.2 Å/mm. The f-number is equal to F/3.2. The instrumental function that takes into account distortions introduced by the input slit, lenses, and the diffraction grating was obtained for a similar spectrometer in [30]. The contour of the instrumental function was obtained for the slit width of 400 μm that is equal to the core diameter of the optical fiber in the model under consideration and is illustrated in Fig. 22. The full width at half-maximum of the contour equals 1.9 Å, which is much less than the width of the spectral lines obtained as a result of simulation. Hence, the detected spectrum changes only slightly by the spectrometer. The largest influence of spectrometer was visible in the spectrum calculated for the peripheral observation chord. The convolution for this chord is presented in Fig. 23 as an example. It can be seen that taking the instrumental

Table 1. Characteristics of lenses used for simulation of light collection for LOS 1

Parameter	Spectral range	Diameter	Focal length	f-number	Radius of curvature of front surface	Radius of curvature of back surface
Lens A	400–700 nm	75 mm	200 mm	F/2.67	96.37 mm	118.81 mm
Lens B	400–700 nm	75 mm	200 mm	F/2.67	288.97 mm	–96.37 mm

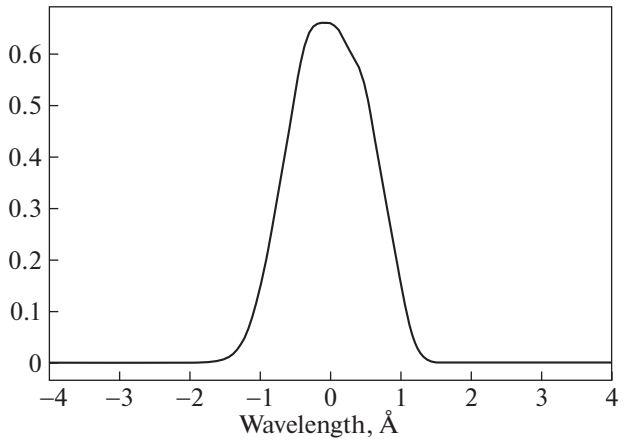

Fig. 22. Instrumental contour of spectrometer used in the simulation.

contour into account made the spectrum smoother but did not result in line overlap.

Having taken the influence of the spectral device into account, we integrated the spectrum convoluted with the instrumental contour of the spectrometer over the camera matrix. The EMCCD camera with a resolution of 512 × 512 pixels 24 μm each and quantum efficiency of 90% was chosen for the simulation. The total transmission of entire system from the input faces of the optical waveguides to the output lens of the spectrometer was set equal to 7%, which corresponds to expected transmission of similar systems at other facilities [35]. The number of counts per second that will be detected by the camera in this case for the chords under consideration is presented in Fig. 24.

Statistical noise in the form of a random quantity characterized by normal distribution of the probability density, the mean value equal to zero, and standard deviation equal to the square root of the signal amplitude at a given point of the matrix was added to the signals in the camera frames with and without the active signal. Using the algorithm of the time difference scheme, a difference signal containing only the active signal with noise was retrieved from the noisy signals of the matrix. The difference signals for the chosen chords obtained with integration time of 50 ms are presented in Fig. 25. It is evident from the figure that the signal level obtained along the central observation chord with the specified exposure time was relatively low and contained much noise. The signal-to-noise ratio was considerably higher for the central and the peripheral chords.

7. ANALYSIS OF PARAMETERS OF THE MSE MEASUREMENTS

To estimate the efficiency of measuring plasma parameters using the MSE-LS technique, we estimated the spatial and temporal resolution that can be expected upon realization of the MSE diagnostic according to the concept presented in this work.

The spatial resolution was estimated as the distance in the radial direction between the outer and inner magnetic surfaces that the line of sight crosses at the entering and exiting of the diagnostic beam, where the input and output points are determined by the effective beam diameter. The estimated spatial resolution for collection systems LOS 1 and LOS 4 is presented in Fig. 26. Several factors determine the obtained values. First, the necessity of arranging the lines of sight at a large angle relative to the beam in order to shift the active spectrum relative to the passive one. Second, the relatively large diameter of the diagnostic beam (about 12 cm) and its injection direction. The possibility of beam observation in the poloidal direction or rotation of the injection axis with respect to toroidal angle should be considered for achieving a higher spatial resolution.

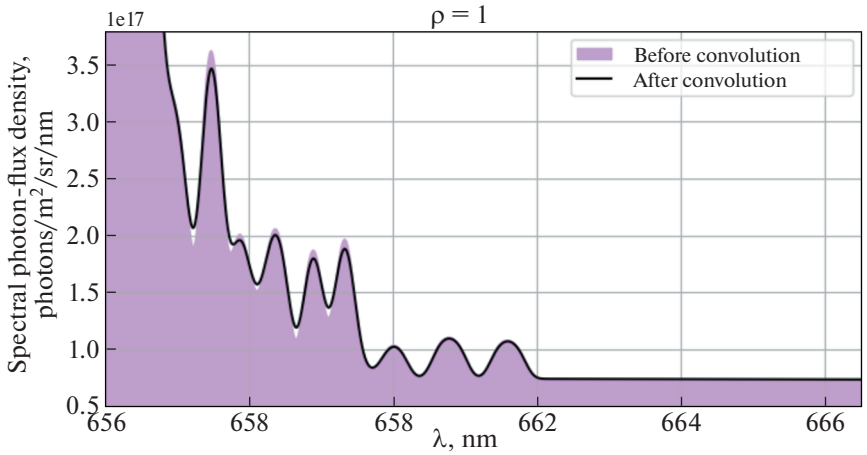

Fig. 23. Comparison of simulated spectra obtained before and after spectrometer.

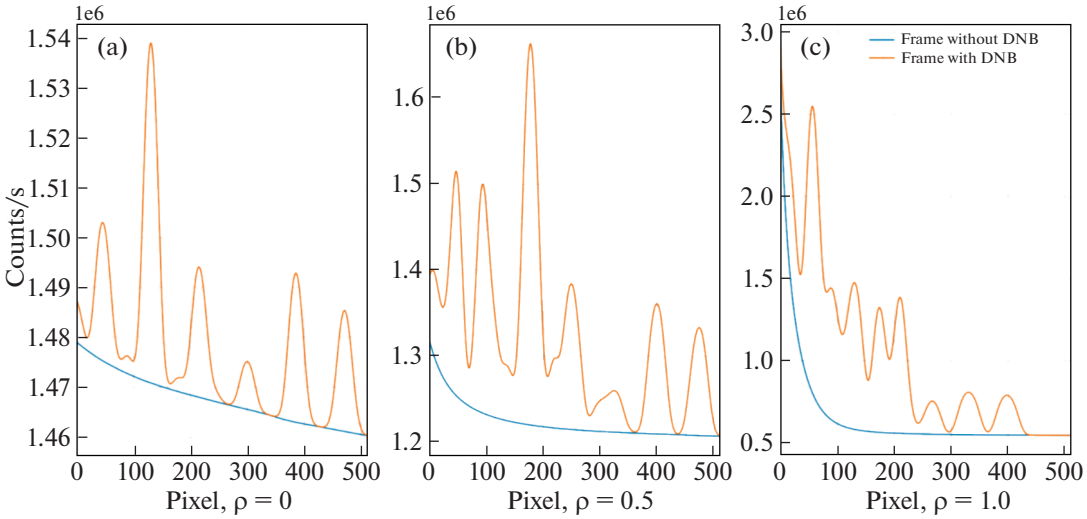

Fig. 24. Frames containing active and passive spectra on the camera matrix for three lines of sight.

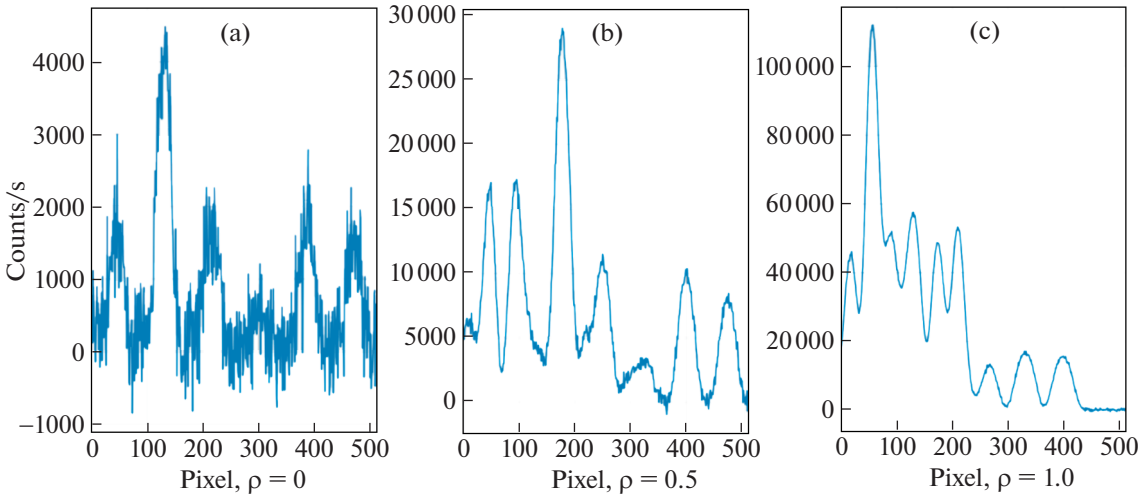

Fig. 25. Difference signal for exposure time of 50 ms.

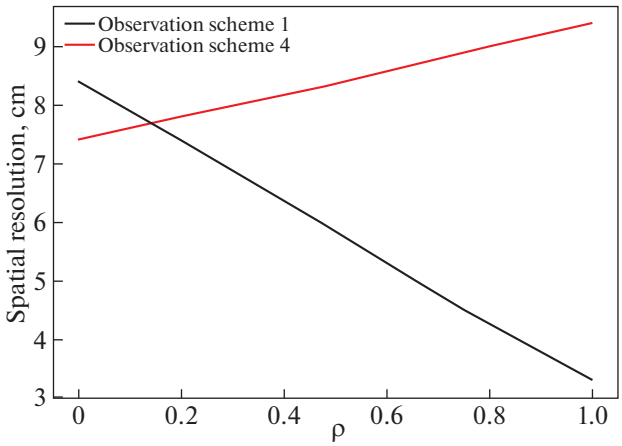

Fig. 26. Estimated spatial resolution of the MSE measurements.

To determine the temporal resolution that can be achieved using the diagnostic equipment with components and characteristics presented in this part of the report, we calculated the dependence of the signal-to-noise ratio (SNR) for the discussed chords as a function of exposure time. The SNR was defined as the ratio of half-maximum of the brightest line of the active spectrum on the sensor to standard deviation of the overlapped noise. The results of the calculation are presented in Fig. 27. It can be seen that the SNR for the central line of sight falls in the range of 2–14, while that for the lines of sight aimed at $\rho = 0.5$ and $\rho = 1$ is one to two orders of magnitude larger. The temporal resolution of the MSE diagnostic for given signal-to-noise ratio appears to be different for each line of sight, which also testifies in favor of separating the detection system into several parts with respect to areas of the

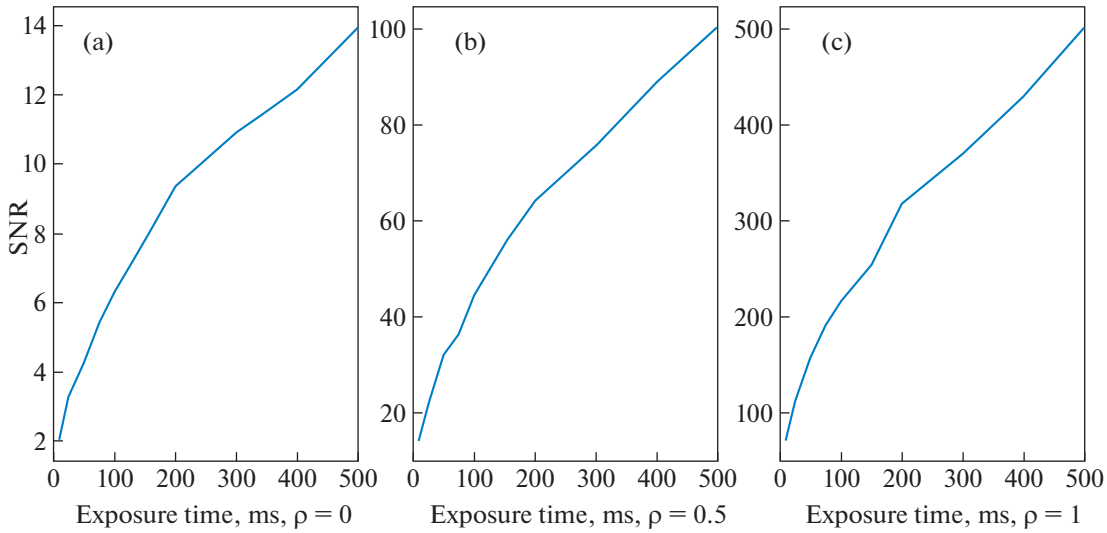

Fig. 27. Signal-to-noise ratio as a function of exposure time.

plasma column they observe. Assuming that the SNR of 5 is sufficient for determining the plasma parameters with required accuracy along the central chord, the temporal resolution of the diagnostic is expected to be at the level of 65 ms.

CONCLUSIONS

To formulate the concept of the MSE diagnostic for the TRT tokamak, we simulated the MSE spectra and the accompanying background signals taking into account reflections of radiation from the inner surfaces of the vacuum vessel. Based on the results of analysis of the simulated spectra, we proposed the schemes of arrangement of the light-collection systems and parameters of collecting optics: the angles of view, focal lengths, and numerical apertures. Positions of the diagnostic injector relative to the heating ones were determined, along with the lower bound of the energy of the diagnostic-beam main component (70 keV) for which the MSE spectrum can be shifted sufficiently relative to the passive D_α line of plasma that is dominated by the reflected radiation from the divertor. The difference signal for the high-transmission spectral device with an f-number of F/3.2 and scientific EMCCD camera was obtained. The spatial and temporal resolution of the diagnostic were estimated to be 6–8 cm and 65 ms, respectively.

ACKNOWLEDGMENTS

The MSE spectra were simulated using computing resources of the federal collective usage center Complex for Simulation and Data Processing for Mega-Science Facilities at the National Research Centre "Kurchatov Institute," http://ckp.nrcki.ru/.

FUNDING

This work was funded by the Contract no. 1770641334823000044O/53-23/01/230/22-23 dated June 28, 2023, between Institution "Project center ITER" and National Research Centre "Kurchatov Institute" in the frame of Government contract no. N.4k.241.09.23.1060 dated April 17, 2023.

CONFLICT OF INTEREST

The authors of this work declare that they have no conflicts of interest.

REFERENCES

1. A. V. Krasilnikov, S. V. Konovalov, E. N. Bondarchuk, I. V. Mazul', I. Yu. Rodin, A. B. Mineev, E. G. Kuz'min, A. A. Kavin, D. A. Karpov, V. M. Leonov, R. R. Khairutdinov, A. S. Kukushkin, D. V. Portnov, A. A. Ivanov, Yu. I. Belchenko, et al., Plasma Phys. Rep. **47**, 1092 (2021).
2. F. M. Levinton, R. J. Fonck, G. M. Gammel, R. Kaita, H. W. Kugel, E. T. Powell, and D. W. Roberts, Phys. Rev. Lett. **63**, 2060 (1989).
3. V. A. Krupin, S. N. Ivanov, A. A. Medvedev, T. B. Myalton, V. S. Strelkov, and V. A. Chaklin, Preprint IAE-5940/7 (NRC Kurchatov Institute, Moscow, 1995).
4. H. Y. Chang, PhD Thesis (Massachusetts Inst. Technol., Cambridge, MA, 2005).
5. J. Chung, J. Ko, J. Howard, C. Michael, G. von Nessi, and A. Thorman, J. Korean Phys. Soc. **65**, 1257 (2014).
6. R. C. Wolf, A. Bock, O. P. Ford, R. Reimer, A. Burckhart, A. Dinklage, J. Hobirk, J. Howard, M. Reich, and J. Stober, J. Instrum. **10**, P10008 (2015).
7. Yu. I. Galushkin, Astron. Zh. **14**, 301 (1970).

8. M. Carr, A. Meakins, M. Bernert, P. David, C. Giroud, J. Harrison, S. Henderson, B. Lipschultz, F. Reimold, EUROfusion MST1 Team, and ASDEX Upgrade Team, Rev. Sci. Instrum. **89**, 083506 (2018). https://doi.org/10.1063/1.5031087; Cherab's Documentation. https://www.cherab.info/. Cited November 20, 2023.
9. A. Meakins, M. Carr, raysect/source: v0.7.0 Release (Version v0.7.0), Zenodo, 2020. https://doi.org/10.5281/zenodo.1341346
10. H. P. Summers, The ADAS User Manual, version 2.6, 2004.
11. O. Marchuk, Yu. Ralchenko, R. K. Janev, W. Biel, E. Delabie, and A. M. Urnov, J. Phys. B: At., Mol. Opt. Phys. **43**, 011002 (2010).
12. M. von Hellermann, M. de Bock, O. Marchuk, D. Reiter, S. Serov, and M. Walsh, Atoms **7**, 30 (2019). https://doi.org/10.3390/atoms7010030
13. A. Blom and C. Jupén, Plasma Phys. Controlled Fusion **44**, 1229 (2002). https://doi.org/10.1088/0741-3335/44/7/312
14. A. S. Kukushkin, H. D. Pacher, V. Kotov, G. W. Pacher, and D. Reiter, Fusion Eng. Des. **86**, 2865 (2011). https://doi.org/10.1016/j.fusengdes.2011.06.009
15. B. A. Lomanowski, A. G. Meigs, R. M. Sharples, M. Stamp, C. Guillemaut, and JET Contributors, Nucl. Fusion **55**, 123028 (2015). https://doi.org/10.1088/0029-5515/55/12/123028
16. T. Ida, M. Ando, and H. Toraya, J. Appl. Crystallogr. **33**, 1311 (2000). https://doi.org/10.1107/s0021889800010219
17. I. H. Hutchinson, *Principles of Plasma Diagnostics*, 2nd ed. (Cambridge Univ. Press, Cambridge, 2002). https://doi.org/10.1017/CBO9780511613630
18. M. A. de Avillez and D. Breitschwerdt, Astron. Astrophys. **580**, A124 (2015).
19. T. R. Carson, Astron. Astrophys. **189**, 319 (1988).
20. G. V. Pereverzev and P. N. Yushmanov, Report No. IPP 5/98 (Max-Planck-Institut Für Plasmaphysik, Garching, 2002). https://w3.pppl.gov/~hammett/work/2009/Astra_ocr.pdf.
21. V. M. Leonov, S. V. Konovalov, V. E. Zhogolev, A. A. Kavin, A. V. Krasilnikov, A. Yu. Kuyanov, V. E. Lukash, A. B. Mineev, and R. R. Khairutdinov, Plasma Phys. Rep. **47**, 1107 (2021).
22. R. L. Cook and K. E. Torrance, ACM Trans. Graphics **1**, 7 (1982). https://doi.org/10.1145/357290.357293
23. J. Karhunen, M. Carr, J. R. Harrison, B. Lomanowski, I. Balboa, P. Carvalho, M. Groth, A. Huber, G. F. Matthews, A. Meakins, S. Silburn, and JET Contributors, Rev. Sci. Instrum. **90**, 103504 (2019). https://doi.org/10.1063/1.5118885
24. V. S. Neverov, R. I. Khusnutdinov, A. G. Alekseev, M. Carr, M. De Bock, A. B. Kukushkin, J. Lovell, A. Meakins, R. Pitts, A. R. Polevoi, and E. Veshchev, Plasma Phys. Controlled Fusion **62**, 115014 (2020). https://doi.org/10.1088/1361-6587/abb53b
25. K. H. Berkner, R. V. Pyle, and J. W. Stearns, Nucl. Fusion **15**, 249 (1975).
26. N. V. Stupishin, P. P. Deichuli, A. A. Ivanov, A. G. Abdrashitov, G. F. Abdrashitov, V. V. Rashenko, P. V. Zubarev, A. I. Gorbovsky, V. V. Mishagin, V. A. Kapitonov, V. A. Krupin, and G. N. Tilinin, in *Proceedings of the 11th International Conference on Open Magnetic Systems for Plasma Confinement, Novosibirsk, 2016*, p. 49.
27. E. Delabie, M. Brix, C. Giroud, R. J. E. Jaspers, O. Marchuk, M. G. O' Mullane, Yu. Ralchenko, E. Surrey, M. G. von Hellermann, K. D. Zastrow, and JET-EFDA Contributors, Plasma Phys. Controlled Fusion **52**, 125008 (2010).
28. K. Jakubowska, M. De Bock, R. Jaspers, M. von Hellermann, and L. Shmaenok, Rev. Sci. Instrum. **75**, 3475 (2004).
29. R. Reimer, Doctoral Thesis (Ernst-Moritz-Arndt-Universität, Greifswald, 2017).
30. L. A. Klyuchnikov, V. A. Krupin, M. R. Nurgaliev, A. R. Nemets, I. A. Zemtsov, S. N. Tugarinov, and N. N. Naumenko, Rev. Sci. Instrum. **88**, 093508 (2017). https://doi.org/10.1063/1.5001490
31. I. U. Uzun-Kaymak, R. J. Fonck, and G. R. McKee, Rev. Sci. Instrum. **83**, 10D526 (2012). https://doi.org/10.1063/1.4733548
32. C. T. Holcomb, M. A. Makowski, R. J. Jayakumar, S. A. Allen, R. M. Ellis, R. Geer, D. Behne, K. L. Morris, L. G. Seppala, and J. M. Moller, Rev. Sci. Instrum. **77**, 10E506 (2006). https://doi.org/10.1063/1.2235812
33. A. Listopad, V. Davydenko, A. Ivanov, V. Mishagin, J. Coenen, V. Savkin, G. Shulzhenko, and R. Uhlemann, Rev. Sci. Instrum. **83**, 02B707 (2012).
34. Yu. I. Belchenko, A. V. Burdakov, V. I. Davydenko, A. I. Gorbovskii, I. S. Emelev, A. A. Ivanov, A. L. Sanin, and O. Z. Sotnikov, Plasma Phys. Rep. **47**, 1151 (2021).
35. V. Krupin, I. Zemtsov, M. Nurgaliev, L. Klyuchnikov, A. Nemets, A. Ivanov, N. Stupishin, N. Naumenko, and S. Tugarinov, J. Instrum. **15**, C02027 (2020). https://doi.org/10.1088/1748-0221/15/02/C02027